GRATING BASED PLASMONIC CAVITIES

A THESIS
SUBMITTED TO THE DEPARTMENT OF PHYSICS
AND THE INSTITUTE OF ENGINEERING AND SCIENCE
OF BILKENT UNIVERSITY
IN PARTIAL FULFILLMENT OF THE REQUIREMENTS
FOR THE DEGREE OF
MASTER OF SCIENCE

By
Servet Seçkin Şenlik
July, 2009

I certify that I have read this thesis and that in my opinion it is fully adequate, in scope and in quality, as a thesis for the degree of Master of Science.

Prof. Dr. Atilla Aydınlı (Advisor)

I certify that I have read this thesis and that in my opinion it is fully adequate, in scope and in quality, as a thesis for the degree of Master of Science.

Assoc. Prof. Dr. Oğuz Gülseren

I certify that I have read this thesis and that in my opinion it is fully adequate, in scope and in quality, as a thesis for the degree of Master of Science.

Prof. Dr. Ömer Dağ

Approved for the Institute of Engineering and Science:

Prof. Dr. Mehmet B. Baray
Director of the Institute

ABSTRACT

GRATING BASED PLASMONIC CAVITIES

Servet Seçkin Şenlik
M.S. in Physics
Supervisor: Prof. Dr. Atilla Aydınlı
July, 2009

Surface plasmon polaritons are dipole carrying electromagnetic excitations occuring at metal-dielectric interfaces. Metallic periodic structures exhibit modified transmission and reflection spectra owing to the interaction of propagating SPPs with the periodicity. These periodic surfaces are used to demonstrate localization of propagating SPPs. Thin metallic films surrounded by Bragg reflectors, selective loading of biharmonic metallic surfaces and Moire patterns are used to demonstrate plasmonic cavity formation. The quality factor, Q, a characteristic value that indicates rate of energy loss relative to the stored energy in the cavity is a crucial parameter for classifying these cavities. It was proposed that the Q factor should strongly depend on the surface geometry. However, there was not a sytematic study on the Q factor of these cavity structures. In this work, we report on a comparative study of grating based plasmonic band gap cavities. Numerically, we calculate the quality factors of the cavities based on three types of grating surfaces; uniform, biharmonic and Moirè surfaces. Experimentally, we demonstrate the existence of plasmonic cavities based on uniform gratings. Effective index perturbation and cavity geometries are obtained by additional dielectric loading. Furthermore, we fabricate 2D plasmonic structures, observe plasmonic band gaps in the symetry axis and propose cavity geometries for this structure.

Keywords: Surface plasmon polaritons, Localization, Biharmonic gratings, Uniform gratings, Moirè surface, Cavity, Quality factor.

ÖZET

KIRINIM AĞI TABANLI PLAZMONİK KOVUKLAR

Servet Seçkin Şenlik
Fizik Bölümü, Yüksek Lisans
Tez Yöneticisi: Prof. Dr. Atilla Aydınlı
Temmuz, 2009

Yüzey plazmon polaritonları, metal-dielektrik yüzeylerinde hareket eden çiftkutup taşıyan elektromanyetik hareketlenmelerdir. Metalik periyodik yüzeyler hareket eden yüzey plazmon polaritonları ile etkileşerek o yüzeylerin geçirgenlik ve yansıtma özelliklerini değiştirir. Bu periyodik yüzeyler hareket eden yüzey plazmon polaritonların yerelleştirilmesinde kullanılmaktadırlar. Bragg yansıtıcıları tarafından çevrelenmiş ince metal kaplamalar, çift periyotlu metalik kırınım ağlarının tercihli kaplanması ve Moire yüzeyleri plazmonik kovukların gösterilmesinde kullanılmıştır. Kalite faktörü kovuklardaki enerji kaybının depolanan enerjiye oranıdır ve plazmonik kovukları sınıflandırmada önemli bir özelliktir. Kalite faktörünün yüzey geometrisine bağlılığı öne sürülmüş ama sistematik bir çalışma yapılmamıştır. Bu tezde kırınım ağı tabanlı plazmonik kovukların kalite faktörlerine ilişkin bir çalışma yapılmıştır. Sayısal olarak, tek periyotlu, çift periyotlu kırınım ağları ve Moire yüzeylerindeki plazmonik kovukların kalite faktörleri hesaplanmıştır. Deneysel olarak, tek periyotlu kırınım ağları üstünde plazmonik kovuk oluşumu gösterilmiştir. Ayrıca, iki boyutlu plazmonik bant aralığı yapıları üretilmiştir ve bu yapılar için kovuk geometrisi önerilmiştir.

Anahtar sözcükler: Yüzey plazmon polaritonları, Yerleşme, Çift periyotlu kırınım ağları, Tek periyotlu kırınım ağları, Moire yüzeyleri, Kovuk, Kalite faktörü.

Acknowledgement

I would like to express my indebtedness to my academic supervisor Prof. Atilla Aydınlı for his encouragement and guidance.

I would like to thank Dr. Aşkın Kocabaş for introducing me surface plasmons and teaching his experience in laboratory.

I would also like to thank my thesis committe, Prof. Ömer Dag̃ and Prof. Oğuz Gülseren for their reading and commenting on this thesis.

I would like to thank my group mates Samed Yumrukçu, Ertuğrul Karademir and Mustafa Karabıyık for valuable discussions and their friendships. I would like to thank to Ertuğrul once more for his technical support and I would also like to thank Dr. Mecit Yaman for his critical reading of this work.

I would like to thank Ahmet Keleş for his sincere friendship and especially his motivation talks. I would like to thank H. Esat Kondakçı for his friendship and support.

I am indepted to Tuncay Özel and Samed Yumrukçu (a.k.a 2+1) for their friendships and support during my seven years in Bilkent. Their support is invaluable for me.

I wish to express my attidues to Mustafa İncebacak (a.k.a Musti) for his endless friendship and İncebacak family for their support (F2-49).

I wish to express my special thanks to my parents, my elder brother Niyazi and my aunt for their support and love.

I wish to express my deepest graditudes to my wife, Özlem for always being near myself. Without her support, encouragment and love, this work would be impossible.

The financial support from Turkish Scientific and Technical Research Council (TUBITAK) is also gratefully acknowledged.

in loving memory of my mother

Contents

List of Figures

List of Tables

Chapter 1

Introduction

Despite the fact that surface plasmon polaritons (SPP) have been known for half a century, there have been a renewed interest in this field during the last decade. The reason behind this interest is the observation that SPPs help to concentrate and guide the light in subwavelength stuructures. In optical devices this limit cannot be reached due to the diffraction limit [1] [2].Furthermore, recent developments in the fabrication of nanometer scale structures enable controlling SPP properties. This control brings new understanding in SPP physics and makes them suitable for specific applications. The use of SPPs in concentaring light results in massive electric field enhancements at these structures. This enhancement is used in surface enhanced Raman spectroscopy which enables detecting a single molecule [3][4]. SPPs are used in biological sensing applications for many years[5][6]. Thus, SPP field is an interdisciplinary area where both physicist, chemists, material scientist and biologists work.

Studying the confinement behavior of surface plasmon polaritons is important as it advances understanding of SPP physics as well as its technological applications. In this regard, localization of SPPs using Bragg mirrors have been studied, recently. Both experimental and numerical demonstration of plasmonic cavities on different surface geometries are achieved. The quality factor, Q,-a characteristic value that indicates rate of energy loss relative to the stored energy of the cavity is a crucial parameter for characterizing the confinement properties of these cavities. It was proposed that the Q factor should strongly depend on the surface geoemtry. However, there has not been a sytematic study on the Q factor of these cavity structures. In this work, we report on a comparative study of grating based plasmonic band gap cavities. Numerically, we calculate the quality factors of the cavities based on three types of grating surfaces; uniform, biharmonic and Moir surfaces. Experimentally, we demonstrate the existence of plasmonic cavities based on uniform gratings. Effective index perturbation and cavity geometries are obtained by additional dielectric loading. Furthermore, we show our preliminary study for demonstration of 2D plasmonic cavity structures.

Chapter 2 gives the fundamentals of SPP physics including the dielectric modeling of metals, the charcteristics of SPPs, excitation of SPPs, the behavior of SPPs on flat and periodic surfaces and localization of SPPs in cavities. Chapter 3 reviews the techniques we used to fabricate and characterize plasmonic structures. Chapter 4 represents our results on experimental demonstration of plasmonic cavities on uniform gratings and numerical study on the quality factors of grating based plasmonic cavities. Chapter 5 represent the summary of our study and future work plan in this field.

Chapter 2

Fundamentals of Surface Plasmon Polaritons

Surface plasmon polaritons (SPPs) are dipole carrying electro magnetic excitations that occur due to coupling of photons and collective oscillations of free electrons at the interface between a metal and a dielectric[**?**]. The metal surfaces supply free electrons for the excitation of SPPs. The characteristics of SPPs such as dispersion relation and propagation distance depends on the optical properties of the metal. In this chapter, optical properties of metals, dispersion relation of SPPs, excitation techniques for SPPs and their behavior on periodic surfaces to have a better understanding of the physics involved will be reviewed.

2.1 Optical Properties of Metals

In this section, the basic concepts of dielectric response of metals will be introduced. Plasma model and its validity will be discussed. Then we will show real optical behavior of metals where plasma model fails.

2.1.1 Plasma Model

Plasma model assumes an electron gas of density n which moving in a fixed background of positive ion cores. This model is adequately explains even ultraviolet regime of alkali metals (Na, K, Rb, Cs, Fr), however the interband transitions limits the validity of the model for the noble metals (Ru, Rh,Pd, Ag, Os, Ir, Pt, Au). Details of the lattice potential and electron-electron interaction do not take part in this text. The effect of the lattice potential shows itself as defines an effective optical mass for the electrons[7]. When an alternating electric field is applied, electrons response to it by an oscillatory motion which is damped due to collisions with a characteristic collision frequency of $\gamma = 1/\tau$. τ is also known as relaxation time and for most metals it is of the order of $10^{-14}s$ at room temperature. The equation of motion for an electron sea under an external alternating electric field is E:

$$m\ddot{x} + m\gamma\dot{x} = -eE. \tag{2.1}$$

When the time dependence of the electric field is harmonic, $E(t) = E_0 e^{-iwt}$, a particular solution can be written for the plasma oscillation. $x(t) = x_0 e^{-iwt}$. The phase shift between field and the oscillation is the x_0 term. Solving Eq.2.1 for x(t) we obtain:

$$x(t) = \frac{e}{m(\omega^2 + i\gamma\omega)} E(t). \tag{2.2}$$

The dielectric permitivity is related to the E field by the constituent relations $D = \epsilon E = \epsilon_0 E + P$. The effect of the displaced electron plasma to the polarization term is described by $P(t) = -nex(t)$, where n is the density of electrons in lattice. Combining Eq. 2.2 and expression for P, D can be written as:

$$D = (1 - \frac{\omega_p^2}{\omega^2 + i\gamma\omega})\epsilon_0 E. \tag{2.3}$$

Then the expression for the dielectric function of electron plasma model can be written as:

$$\epsilon(\omega) = (1 - \frac{\omega_p^2}{\omega^2 + i\gamma\omega})\epsilon_0. \tag{2.4}$$

where ω_p is called the plasma frequency. Because the same expression can be obtained by the Drude model it is also referred as optical response of the Drude model[7]. The real and imaginary parts of Eq. 2.4 are:

$$\epsilon(\omega) = \epsilon_1(\omega) + i\epsilon_2(\omega), \tag{2.5}$$

$$\epsilon_1(\omega) = 1 - \frac{\omega_p^2 \tau^2}{1 + \omega^2 \tau^2}, \tag{2.6}$$

$$\epsilon_2(\omega) = \frac{\omega_p^2 \tau}{\omega(1 + \omega^2 \tau^2)}. \tag{2.7}$$

The complex refractive index $\tilde{n}(\omega) = n(\omega) + i\kappa(\omega)$ of the medium can be found from $\tilde{n}(\omega) = \sqrt{\epsilon}$. The real and imaginary parts of refractive index are written as:

$$n(\omega) = \sqrt{\frac{\epsilon_1}{2} + \frac{1}{2}\sqrt{\epsilon_1^2 + \epsilon_2^2}}, \tag{2.8}$$

$$\kappa(\omega) = \frac{\epsilon_2}{2n}. \tag{2.9}$$

where κ is called the extinction coefficient and is a measure of the optical absorption.

The frequency response of the dielectric function can be investigated for high frequency electric fields where $\omega\tau >> 1$ the imaginary part of the dielectric function is negligible and can be written as:

$$\epsilon(\omega) = 1 - \frac{\omega_p^2}{\omega^2}. \tag{2.10}$$

The model fails in this regime for noble metals due to interband transitions which increase loss, leading to high ϵ_2 which cannot be negligible anymore. In the low frequency regime, where $\omega\tau^{-1} << 1$ the imaginary part of the dielectric function is dominant so the real and imaginary part of the refractive indices are comparable in this regime and can be found as

$$n \approx \kappa = \sqrt{\frac{\epsilon_2}{2}} \tag{2.11}$$

Therefore, in the low frequency regime metals are mostly absorptive. The Fig. 2.1 and Fig. 2.2 shows the ϵ and $\tilde{n}$ of silver as a function of energy. The ϵ and $\tilde{n}$ of silver are plotted as a function of energy according to Drude model with $\tau = 1.45 \times 10^{13} s^{-1} (\equiv 0.06eV)$ and $\omega_p = 1.2 \times 10^{16} rads^{-1}$ In Fig 2.1 blue curve represents ϵ_1 and red curve represents ϵ_2. The wine line stands for the plasma frequency. It is clearly seen that ϵ_1 changes sign at ω_p. It is negative below this frequency and positive above it. Above this frequency metal becomes transparent to the applied electric field.

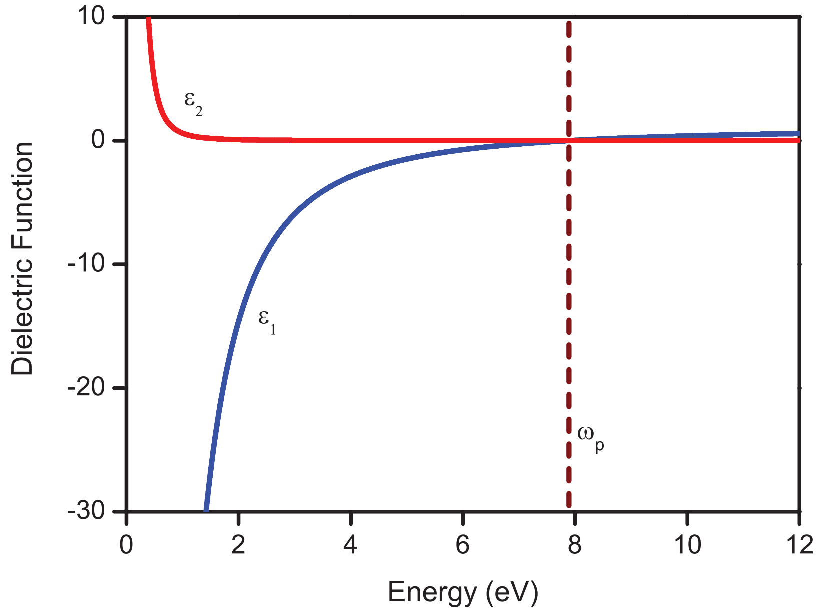

Figure 2.1: Real(ϵ_1) and imaginary(ϵ_2) parts of dielectric functions calculated using Drude model.

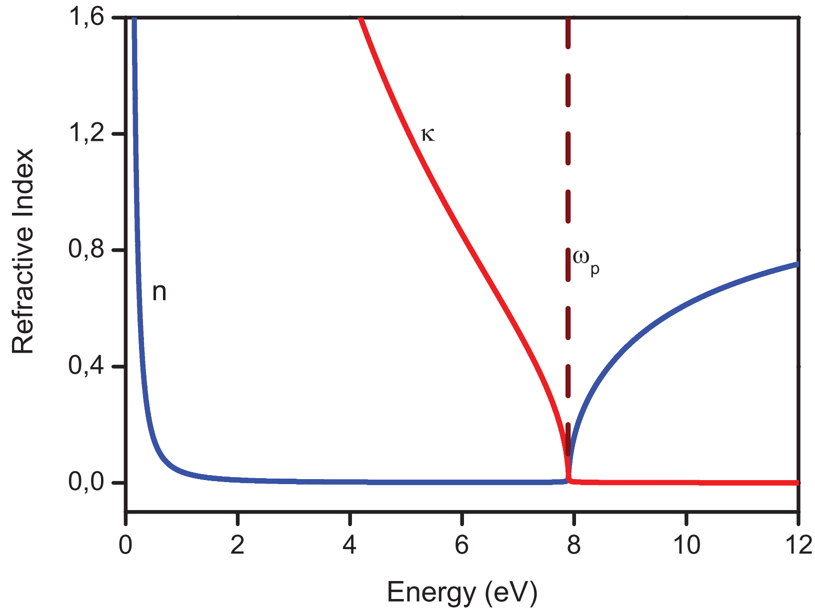

Figure 2.2: Refractive index (blue line) n and extinction coefficients (red line) κ calculated from Drude model.

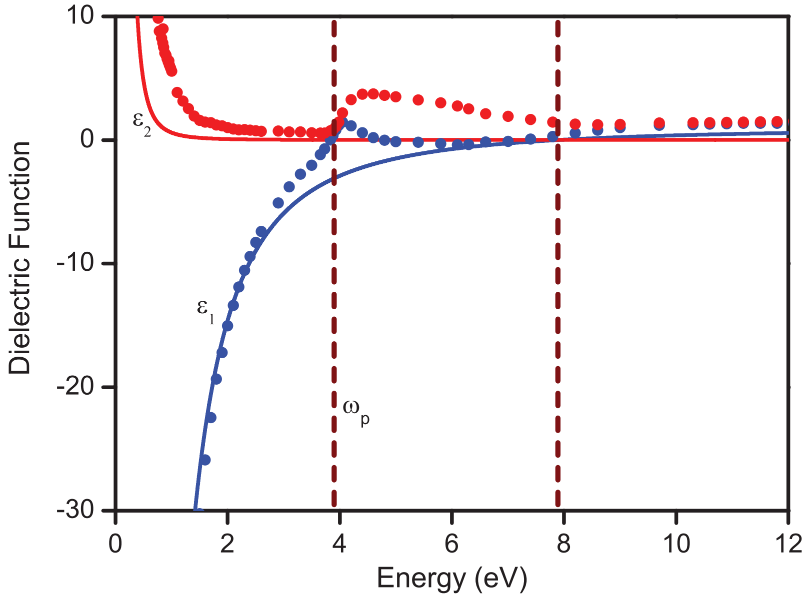

Figure 2.3: Real(ϵ_1) and imaginary(ϵ_2) parts of dielectric functions calculated from Drude model (lines) and experimentally measured values (dots).

2.1.2 Optical Constants of Real Metals

Drude's free electron model fails in the visible and ultra violet regime for noble metals which are materials of choice of many plasmonic applications. Therefore, it is important to describe the dielectric function of the metals accurately. The color of the noble metals are different although Drude model estimates nearly the same plasma frequency corresponding to same color for these metals. The quantum theory explains the difference by the interband transitions occurring between d to sp bands. The electron configuration of gold and silver are $[Xe]4f^{14}5d^{10}6s^1$ and $[Kr]4d^{10}5s^1$, respectively. For silver $4d$ and $5s$ orbitals are just below the Fermi level. The energy difference between orbitals are in the order of $1.1\ eV \sim 1\ \mu m$ shifting the plasma frequency of silver to $3.9\ eV$. The polarized interband excited electrons modify the dielectric behavior resulting in a drop in the reflection spectrum and giving rise the characteristic color of the metal[8]. Fig. 2.3 and Fig. 2.4 shows the difference and similarities between measured values and Drude model calculations of the dielectric function and refractive index. It is clearly seen that the resonance freqeuncy shifts from $7.9\ eV$ to $3.9\ eV$. Practically, Drude model is easily used in to the time-domain based numerical solver such as FDTD

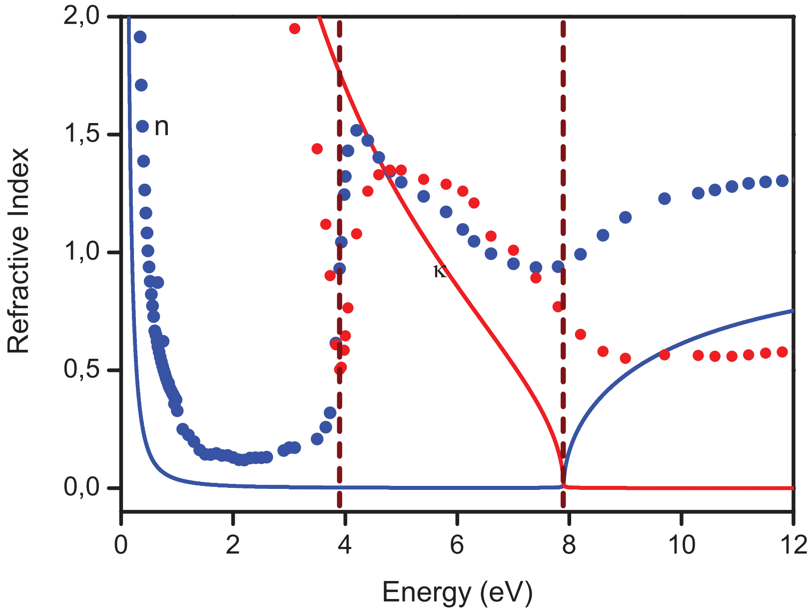

Figure 2.4: Refractive index n and absorbtion coefficients κ calculated from Drude model (Lines) and experimentally measured values(Dots)

since the model allows to write induced current directly[7].

2.2 Characteristics of SPP

In this section, first we will review the derivation of dispersion relation for SPPs and show the field distribution of SPPs. Next, we will review characteristic scales for SPPs as a function of index, wavelength, propagation distance and penetration depths of SPPs.

2.2.1 Dispersion of Surface Plasmon Polaritons

From the wave equation as a start, one can derive the dispersion relation of SPPs from Maxwell equations. Wave equation will be solved in regions with constant dielectric permittivity together with the boundary conditions. To describe the confined wave propagating at the interface first, we will define the geometry and the time dependenceof the field. In Fig. 2.5 the geometry is shown, dielectric

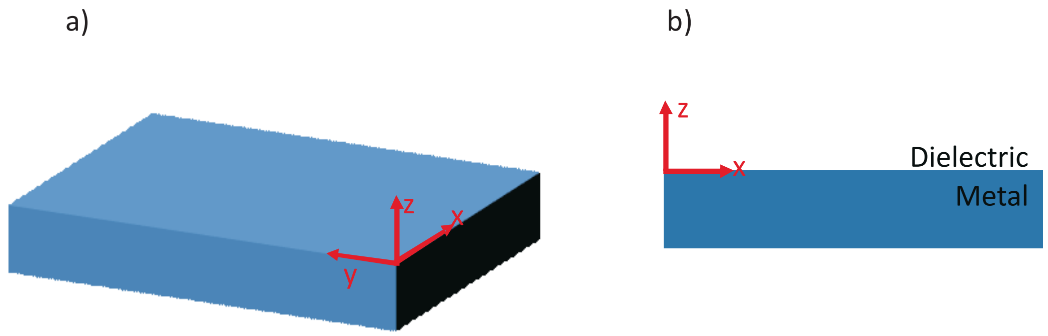

Figure 2.5: a)The propagation geometry. b)xz plane of propagation geometry

permittivity is constant in the xy plane and changing abruptly at $z = 0$. It equals to ϵ_1 above $z = 0$ to ϵ_2 below $z = 0$. x is the propagation direction. The propagating wave can be written as $E(r,t) = E(z)e^{i\beta x}e^{-i\omega t}$ with a harmonic time depence. β is the propagation constant along the x direction. Inserting the expression into the electromagnetic wave equation, we obtain:

$$\frac{\partial^2 E(z)}{\partial z^2} + (k_0\epsilon - \beta^2)E = 0. \tag{2.12}$$

where $k_0 = \frac{\omega}{c}$. A similar equation can be written for H component. Propagation in the x direction and homogeneity in the y direction, $(\frac{\partial}{\partial y} = 0)$ simplifies and decouples equations into two polarizations: TM and TE modes. Here, we show only the solutions for the TM mode,

$$E_x = -i\frac{1}{\omega\epsilon_0\epsilon}\frac{\partial H_y}{\partial z}, \tag{2.13}$$

$$E_x = \frac{\beta}{\omega\epsilon_0\epsilon}H_y, \tag{2.14}$$

$$\frac{\partial^2 H_y}{\partial z^2} + (k_0\epsilon - \beta^2)H_y = 0. \tag{2.15}$$

Now, we write the field components which are propagating along the x direction and are confined to the interface. The field components for $z > 0$ can be written as:

$$H_y(z) = A_2 e^{i\beta x}e^{-k_2 z}, \tag{2.16}$$

$$E_x(z) = iA_2\frac{1}{\omega\epsilon_0\epsilon_2}k_2 e^{i\beta x}e^{-k_2 z}, \tag{2.17}$$

$$E_z(z) = -A_2\frac{\beta}{\omega\epsilon_0\epsilon_2}e^{i\beta x}e^{-k_2 z}. \tag{2.18}$$

For $z > 0$ the solutions are:

$$H_y(z) = A_1 e^{i\beta x} e^{-k_2 z}, \quad (2.19)$$

$$E_x(z) = iA_1 \frac{1}{\omega\epsilon_0\epsilon_2} k_2 e^{i\beta x} e^{-k_2 z}, \quad (2.20)$$

$$E_z(z) = -A_1 \frac{\beta}{\omega\epsilon_0\epsilon_2} e^{i\beta x} e^{-k_2 z}. \quad (2.21)$$

where k_1 and k_2 are both positive and restricts the confined behavior along the z direction. Boundary conditions restricts the continuity of H_y and E_x at $z = 0$ plane and result with:

$$A_1 = A_2 \quad (2.22)$$

$$\frac{k_2}{k_1} = -\frac{\epsilon_2}{\epsilon_1} \quad (2.23)$$

It should be noted that k_1 and k_2 are positive, so the ϵ of the media should be of the opposite sign to satisfy Eq.2.23. These surface waves can only occur at the interface of materials with dielectric constants of opposite sign, such as metal-dielectric interface. On the other hand H_y should also satisfy Eq.2.15, namely:

$$k_1^2 = \beta^2 - k_0^2\epsilon_1, \quad (2.24)$$

$$k_2^2 = \beta^2 - k_0^2\epsilon_2. \quad (2.25)$$

We can combine both Eq. 2.23-2.25 and find the dispersion relation of surface plasmon polaritons as:

$$\beta = k_0\sqrt{\frac{\epsilon_1\epsilon_2}{\epsilon_1 + \epsilon_2}}. \quad (2.26)$$

Dielectric permittivity ϵ for dielectrics is usually constant over a wide range of frequencies compared to metals. On the other hand, metals are very dispersive materials such that ϵ of silver changes dramatically from $-0.6209 + i0.01570$ to $-159.6131 + i15.5259$ for wavelengths in the range of 200 to 2000nm. Also it should be noted that β is always larger than k_0 which indicates the nonradiative behavior of surface plasmon polaritons. Also, due to the difference between k_0 and β, photons cannot directly excite SPPs. Fig. 2.6 shows the dispersion relation according to this expression modelling the dielectric constant of metal according to Drude model. The bounded nature of SPPs can be seen from the dispersion curve relies below the light line. For frequencies above ω_p the dispersion curve

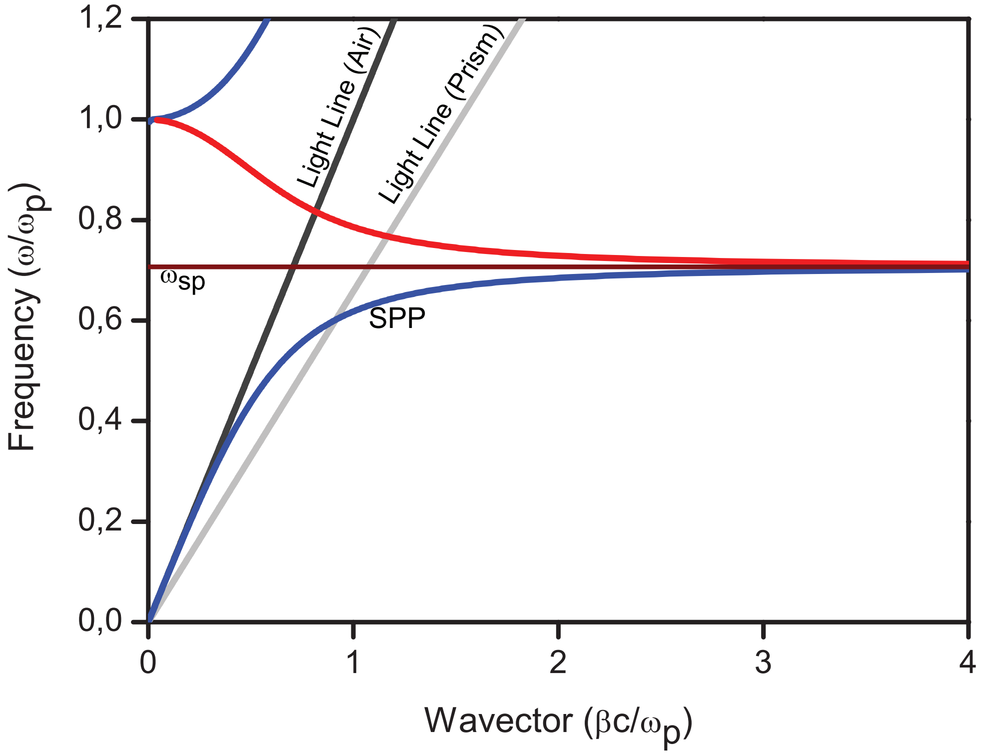

Figure 2.6: Real part of the SPP Dispersion relation at silver-air interface (Blue Line). Imaginary part of the SPP Dispersion relation at silver-air interface.Light line in air (Brown Line) and prism (Gray Line)

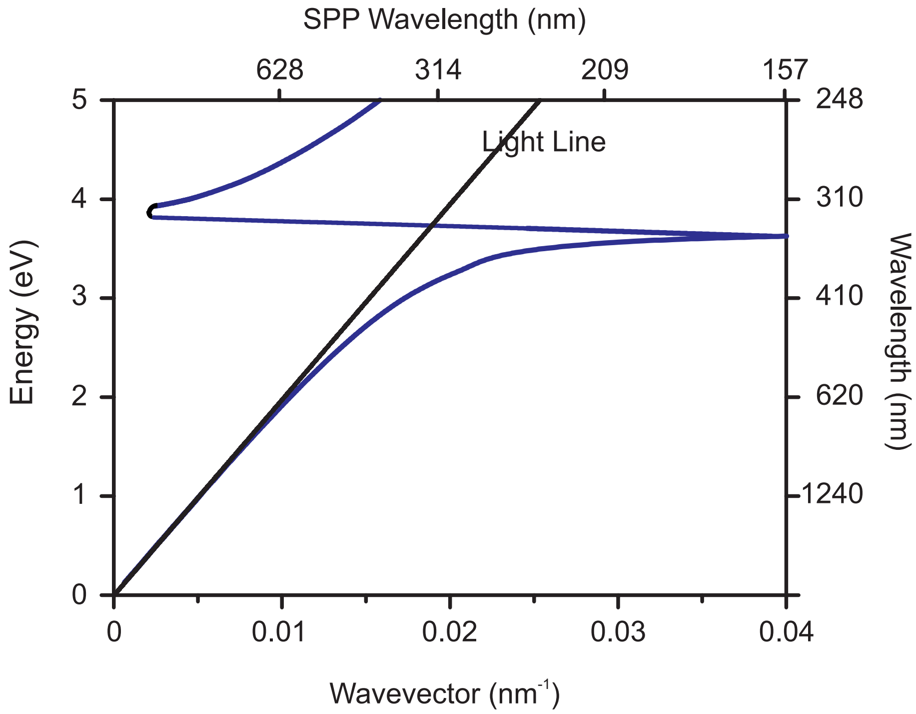

Figure 2.7: The SPP Dispersion relation at silver-air interface (Blue Line)

is above the light line and these modes are called radiative modes. For small wavevectors, propagation constant β and k_0 are very close to each other. For larger wavectors, inserting ϵ of the metal into dispersion relation for SPPs gives us the characteristic surface plasmon frequency, w_{sp}. There is a natural gap between ω_p and ω_{sp} where propagation is not allowed because the propagation constant β takes imaginary values. However, Drude model fails to estimate values of ω_p and ω_{sp} and the behavior between these frequencies.The Fig.2.7 shows the actual relation of SPP with corrected ϵ characteristic of metal. The plasma frequency shifts to 3.9 eV and surface plasmon frequency shifts to 3.7 eV due to additional d orbital transitions. The region between ω_p and ω_{sp} can be experimentally excited and these modes are called as quasi-bounded modes.

2.2.2 Field Distribution of SPP

Fig. 2.8 shows the field distribution of SPPs at the metal-dielectric surface. The electric fields originate from positively charged sites of the metal and end with

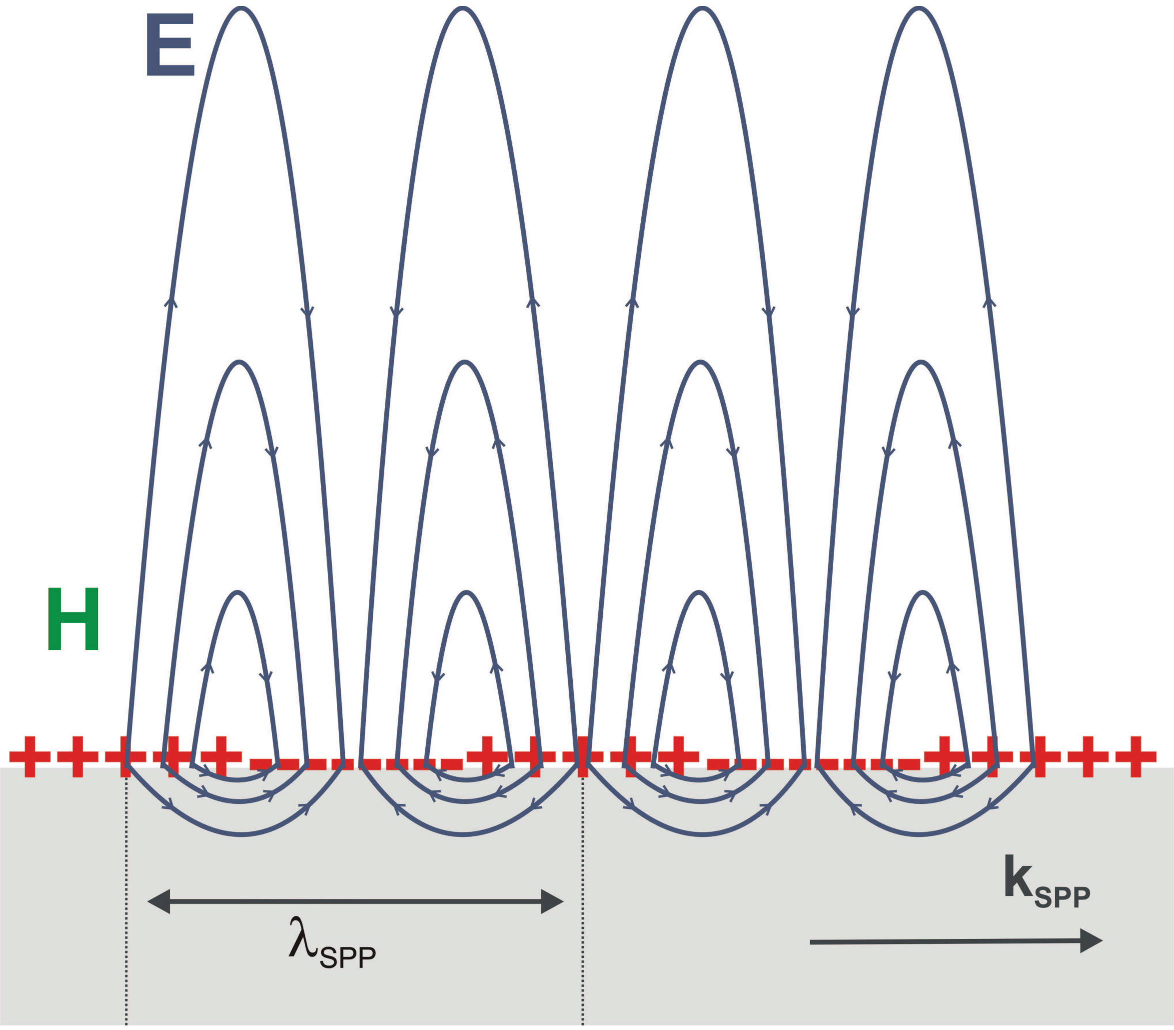

Figure 2.8: Electric and Magnetic field distribution of Surface Plasmon Polariton propagating at metal-air interface (TM case).

the negatively charged sites. Electric field has both parallel and perpendicular components at the interface while H has only paralel components. The direction of perpendicular electric field components in two media are opposite, while the direction of parallel components are the same. The boundary conditions require the continuity of $D_\perp = \epsilon E_\perp$ and $E_\parallel$. Having a metal-dielectric interface with ϵs being negative and positive guarantees the continuity of $D_\perp$ and $E_\perp$. The impossibility of TE polarized SPP is based on absence of magnetic monopoles, resulting in a divergence free H fields. This means that originating and end points of H fields are the same. The H field is divergence free, however boundary condition restricts that $H_\parallel$ should be continous but H have opposite directions at metal dielectric interface due to its divergence free nature. Therefore the TE polarized SPPs cannot fullfill the boundary conditions and can not be excited at metal-dielectric interfaces. A detailed explanation can be found in [9].

2.2.3 The compex refractive Index of SPP

Defining an effective index for SPPs produces a deeper understanding for the bound behavior of SPP. The dispersion relation of SPP can be simplified as $k_{SPP} = \frac{\omega}{c}(1 + \frac{1}{2|\epsilon_{m1}|} + i\frac{\epsilon_{m2}}{2(\epsilon_{m1})^2})$ if $\epsilon_{m2} << |\epsilon_{m1}|$ and $|\epsilon_{m1}| >> 1$. Then the effective index for SPP can be expressed as:

$$n_{SPP} = 1 + \frac{1}{2|\epsilon_{m1}|} + i\frac{\epsilon_{m2}}{2(\epsilon_{m1})^2} \tag{2.27}$$

Note that real part of the n_{spp} is always larger than 1, which indicates the bound baheviour of a SPP. The corresponding momentum for SPP is $p = \hbar k_{SPP}$ is larger than momentum of free photon $p = \hbar k_0$. The imaginary part determines the loss which will be discussed later.

2.2.4 SPP Wavelength

The period of the surface charge density oscillation and field distribution describes the wavelength of SPP. The real and imaginary parts of the dispersion relation

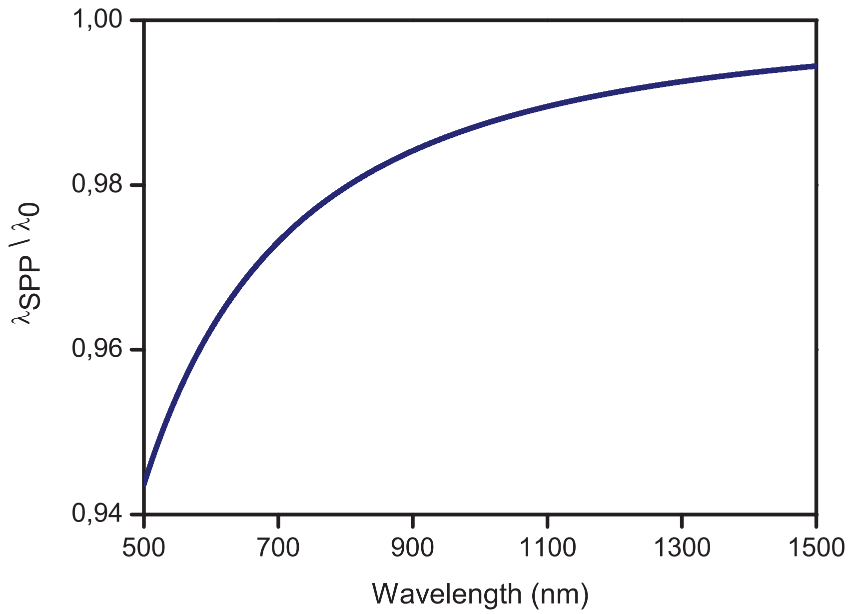

Figure 2.9: Normalized surface plasmon polariton wavelength at silver-air interface. The Drude model is used to characterise silver

describes the wavelength and propagation length of SPP respectively. The real part of the SPP wavevector is

$$k'_{SPP} = k_0\sqrt{\frac{\epsilon_d \epsilon_{m1}}{\epsilon_d + \epsilon_{m1}}}. \tag{2.28}$$

The SPP wavelength can be written from $\lambda_{SPP} = \frac{2\pi}{k_{SPP}}$ and found as:

$$\lambda_{SPP} = \lambda_0\sqrt{\frac{\epsilon_d + \epsilon_{m1}}{\epsilon_d \epsilon_{m1}}}. \tag{2.29}$$

From Fig.2.9 it is seen λ_{SPP} is larger than λ_0. This reduction in the wavelength make SPPs suitable for diffraction limited applications. The wavelength of SPP shrinks to 70 nm at ω_{sp} where the wavelength of a free photon with same energy is 310 nm. In the visible regime this reduction effect is not very important since the ratio of SPP and free photon wavelength is about 0.9 [10].

2.2.5 Propagation Distance of SPP

The main factor reducing propagation distance is the metallic losses. Due to imaginary part of the wavevector in the propagation direction has imaginary

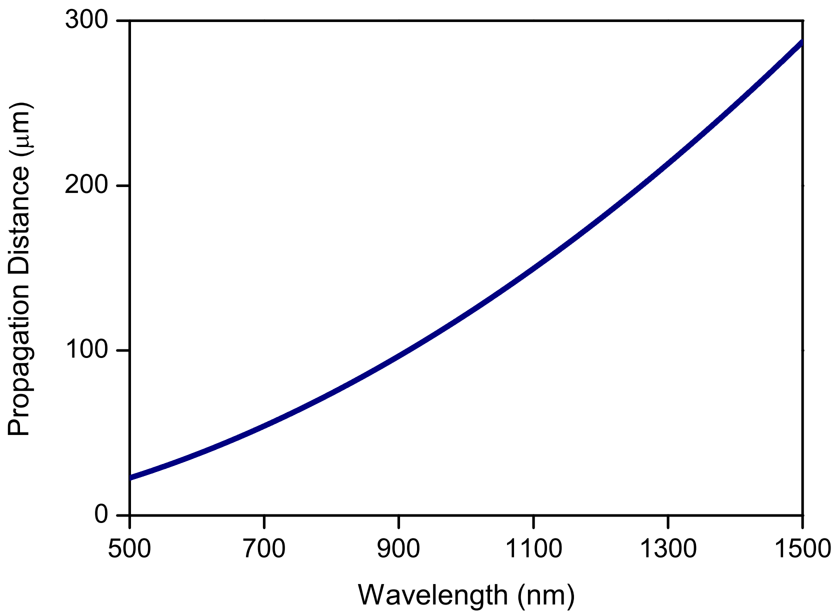

Figure 2.10: The propagation length of the surface plasmon polariton. The Drude model is used to characterise silver

part, the SPP intensity reduces from loss as it propagates. The propagation distance δ_{SPP} can be defined as the length where the power decreases to $1/e$ of value. The propagation distance is defined by $\delta_{SPP} = \sqrt{\frac{1}{2k''_{SPP}}}$ and can be found as[10]:

$$\delta_{SPP} = \lambda_0 \frac{(\epsilon_{m1})}{2\pi\epsilon_{m2}} (\frac{\epsilon_{m1} + \epsilon_d}{\epsilon_{m1}\epsilon_d})^{\frac{3}{2}}. \tag{2.30}$$

The ways to increase propagation distance is to use different geometries for guding of wavelength or using gain media [11].

2.2.6 Penetration Depths of SPP

The SPP field is confined to the interface. It decays into both dielectric and metallic medium. The penetration depths are the length where perpendicular (to interface) component of electric field E_x falls to $1/e$ of its value. It was characterized by k_x which can be found from the expression for total wavevector:

$$\epsilon_i k_0^2 = k_{SPP}^2 + k_{z,i}^2 \tag{2.31}$$

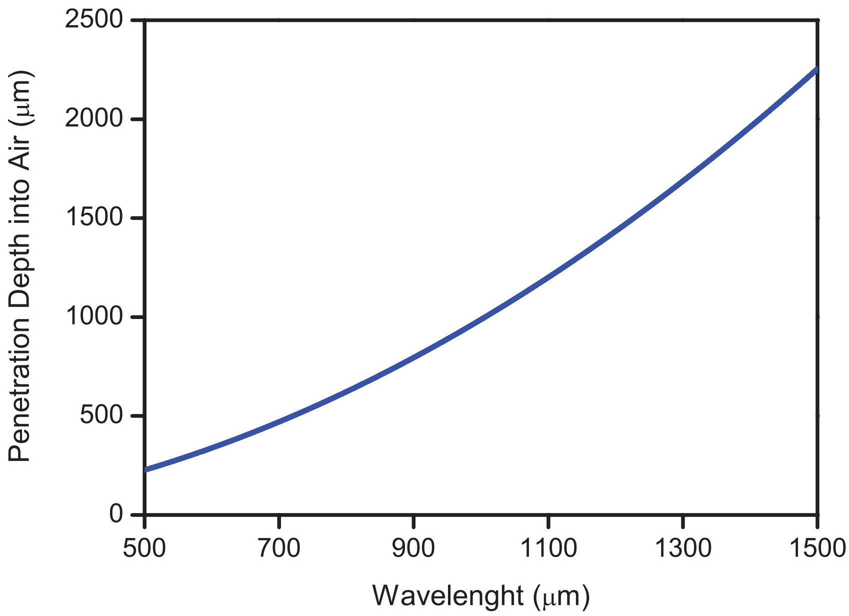

Figure 2.11: The penetration depth of the surface plasmon polariton into air. The Drude model is used to characterise silver

where ϵ_i stands for dielectric constants of metal and dielectric mediums. Then inserting Eq. 2.26 into Eq. 2.31 we can define penetration depths in metal and dielectric as δ_m and δ_d:

$$\delta_m = \frac{1}{k_0 \mid \frac{\epsilon_{m1}+\epsilon_d}{\epsilon_m^2} \mid^{\frac{1}{2}}}, \tag{2.32}$$

$$\delta_d = \frac{1}{k_0 \mid \frac{\epsilon_{m1}+\epsilon_d}{\epsilon_d^2} \mid^{\frac{1}{2}}}. \tag{2.33}$$

The details can be found in [10].

The penetration depth in the dielectric and the propagation length decrease as the wavelength decreases. In other words as the filed localizes along the metal-dielectric interface, the metallic increases and propagation distance decreases[10].

2.3 SPP Coupling

As the dispersion relation reveals, SPP dispersion curve lies below the light line. So there is a necessity to use special phase matching techniques to excite SPPs.

There are numerous techniques to excite SPP such as with charged particles, prism couplers grating couplers, near field coupling . The detailed expalanations can be found [7]. Here we will focus on the prism coupling and the grating coupling method.

2.3.1 Prism Coupler

The method is based on attenuated total reflection (ATR) to excite SPP. The configuration is shown in Fig. 4.1a. The prism is a high index prism which can enhance the momentum of the incident photon. The momentum of SPP is larger than k_0 and to excite an SPP, the parallel k vector component of the incoming photon should be equal to k_{spp}. k vector of incoming photon is increased to $n_{prism}k$. The coupling condition is given by:

$$k_{SPP} = k_0 n_{prism} sin(\theta) \tag{2.34}$$

where n_{prism} and θ) are refractive index of the prism and angle of incidence respectively. The resonance condition can be found through scanning the angle of incidence. The reflected beam intensity goes to a minimum when an SPP is excited. Incident light penetrates through the metal/air interface and partially reflects. SPP also reradiates through the prism and the radiated field interfere with each other. The minimum in the reflected spectrum occurs due to destructive interference between the reradiated SPPs and reflected light at prism-metal interface. The metal thickness is important to reach a perfect dip in the reflection spectrum.

2.3.2 Grating Coupler

Gratings can also supply the momentum needed to excite SPPs. Periodic patterns on the surface can increase the momentum of the incoming light. Using this property of gratings SPPs on both sides, above and below a grating can be excited. The coupling condition is given by this condition

$$k_{SPP} = k_0 \cdot sin(\theta) \pm mG \tag{2.35}$$

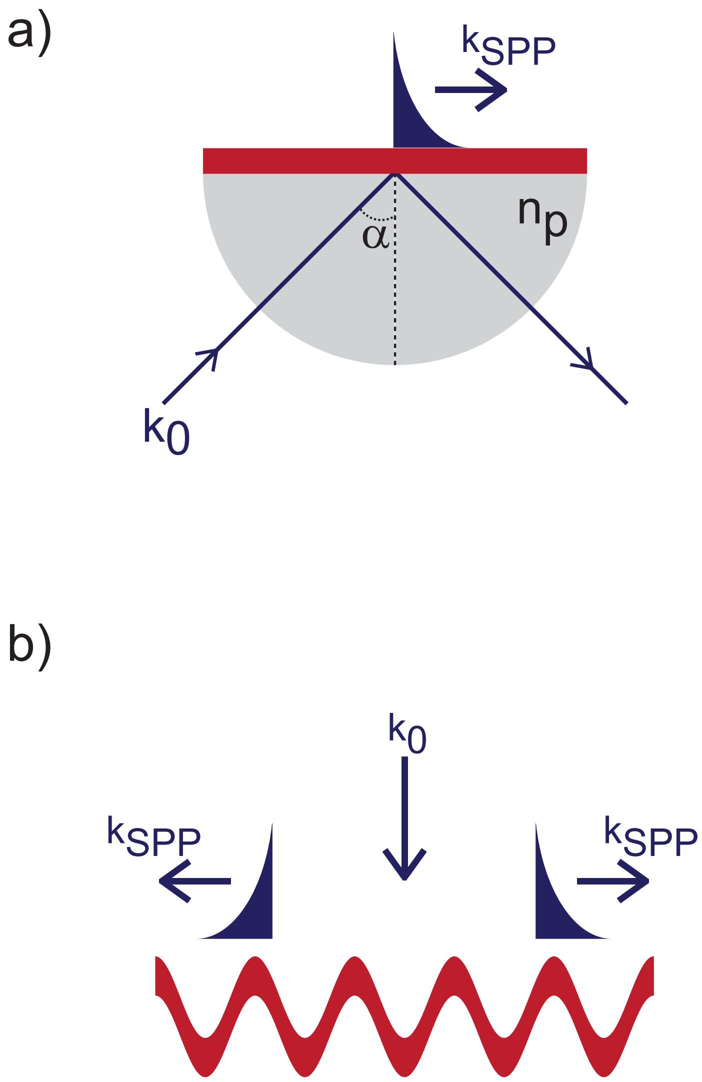

Figure 2.12: a)Prism Coupler. b)Grating Coupler

where θ,$G = \frac{2\pi}{\lambda}$ are angle of incidence of incoming photon and reciprocal vector of the grating respectively with $m = (0, 1, 2...)$. Similarly in the case partially reflected beam and reradiated SPPs interfere destructively and a minima in the reflection spectrum is observed. By changing the incidence angle and wavelength of the photon available, SPP excitations can be measured. The configuration is shown in Fig4.1b.

2.4 Propagation of SPP on Periodic Surfaces

In this section we review the SPP propagation on the periodic surface. We will use the analogy between energy band gaps in condensed matter physics, photonic band gaps in photonic band gap materials and crystals and plasmonic band gaps. In condensed matter physics, energy bands occur due to interaction of the conduction electron with the ion cores of the crystal. At Bragg resonance no wavelike solutions exist. At these wavevectors, left propagating waves are back reflected. The solution of these waves are standing waves and two different standing wave configuration can be constructed. These two standing waves have different spatial distributions and experience different parts of the crystal potentials. One is located on the cores of ions, the other one is between the ion cores. The potential experienced by these two standing waves are different, so the average expected energy values are different for these standing waves. Thus, a band gap is opened between these energies[12]. For the photonic case, media with different refractive indices serve as high and low potential regions for photons. The periodic configuration of this medium is known as photonic crystal. When the light beam is incident onto these structures, there will be scattering at each interface in the structure. If the wavelength of the light is twice the optical periodicity, Bragg condition will be satisfied and the light will be back reflected. These waves will destructively interfere with each other and form a standing wave similar to the electronic case. The configuration of these standing waves will be different. One configuration leads to localization on the high index material and the other on the low index material. There will be energy gap between these values similar to the electronic case, called the photonic band gap[13]. Fig. 2.13 represents

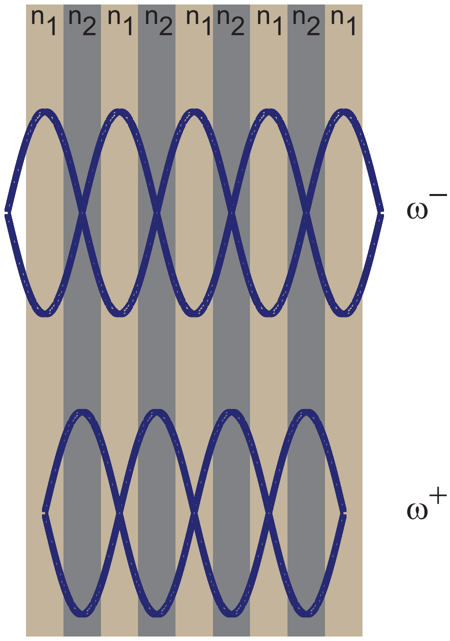

Figure 2.13: Electric field distributions of localised states in the photonic crystal. Lower energy configuration(ω^-). Electric field localizes on the low index regions. Higher energy configuration(ω^+). Electric field localizes in the high index regions

a multilayer dielectric film with high refractive indices (n_2) and low refractive index (n_2). Electric field distribution at edges of band gap are shown in Fig. 2.13. Higher energy configuration standing wave, (ω^+), localizes in high index (n_2) regions and lower energy configuration standing wave, (ω^-), localizes in low index (n_1) regions.

Ion cores for electrons and index difference for photons results in similar effects. In the analogy with electronic band gaps and photonic band gaps, plasmonic band gaps are due to the corrugation of the surface. If the surface where the SPP propagates is peridocally corrugated, the corrugation act as scattering centers since the effective index along the grating changes periodically. The periodic surface leads to scattering of SPPs. When the Bragg condition is met, a band gap opens up. The localized SPPs have different configurations[14]. The Fig. 2.14 represents two electric field distributions of SPPs at the edges of plasmonic band gaps. Siminlar to photonic and electronic case, localization sides of SPP on grating are different for two cases. As seen in Fig. 2.14a the positive and negative charges are localized on the peaks. In the other case, the charges

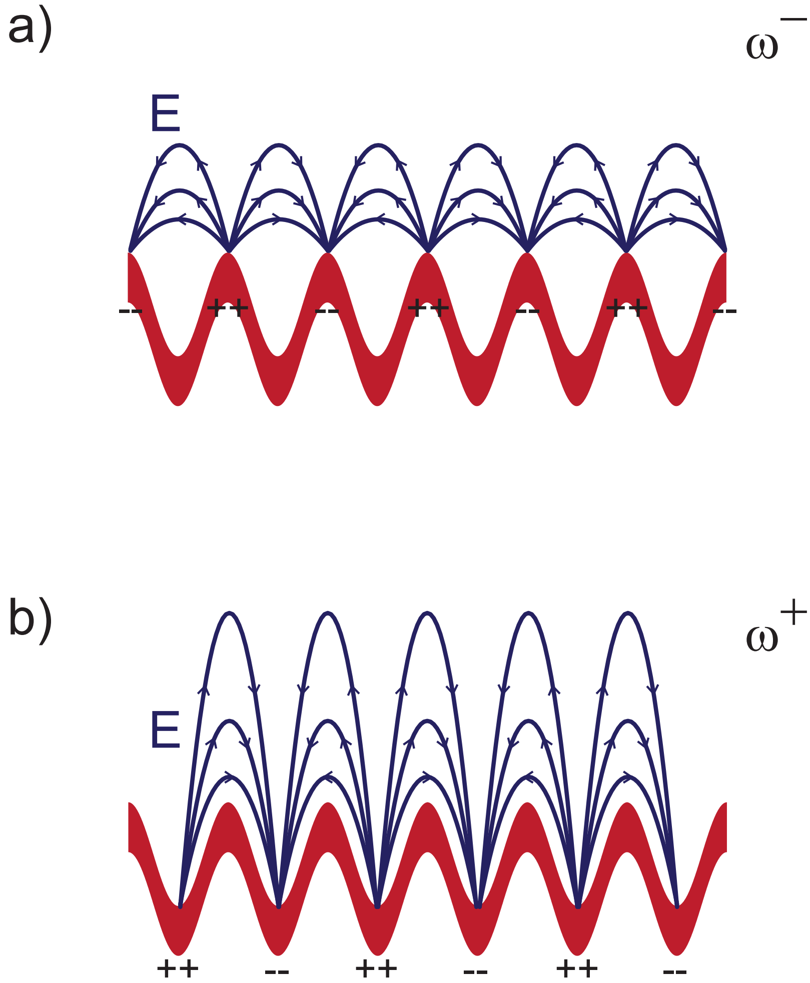

Figure 2.14: Electric field distributions of localised states on the grating. a)Lower energy configuration. Charges localizes on the peaks. b) Higher energy configuration. Charges localizes on the througs.

are localized on the thoughs. The factor that determines the difference in energy of the modes is the distortion in the field lines. Fig. 2.14b represents a more distorted field distribution resulting in a higher energetic mode. Besides the energy difference between these two modes, their confinement behaviors are also different which will be discussed with details in Chapter 5.

2.5 Dispersion of SPP on Periodic Surfaces

There is a momentum mismatch between free space propagating photon and the excited bound plasmon, having the same energy. The dispersion curve for light line lies above the dispersions of bound SPP as seen in Fig. 2.15a. As we discussed in the previous section, excitation of SPP on flat metal surface is forbidden. However, when we consider the dispersion of free photon in prism, its dispersion line lies below the light line in air as seen in Fig. 2.15b. There is a point where dispersion of SPP and dispersion of free photon in prism intersect. SPP can be excited at that point. We can excite SPP resonances by the prism coupling technique discussed above. The Fig. 2.15c shows the dispersion of SPP on a periodic surface. The band gap formation takes place for periodic surfaces at the edges of Brillion zone. However, the dispersion of SPP still lies above the light line , the momentum mismatch condition prohibits the excitation of SPPs. Applying the prism coupler technique, the SPP dispersion in Fig. 2.15c can be observed. The Fig. 2.15d indicates the resulting dispersion curves. The periodic surface is placed on the prism and SPP curve can be observed by scanning the angle of incidence and wavelength.

2.6 Localization of SPP

In this section, we will review the physical principles behind the formation of plasmonic cavities. We will make anology between photonic cavities in photonic crystals and plasmonic cavities. Then, we will show the attempts to demostrate

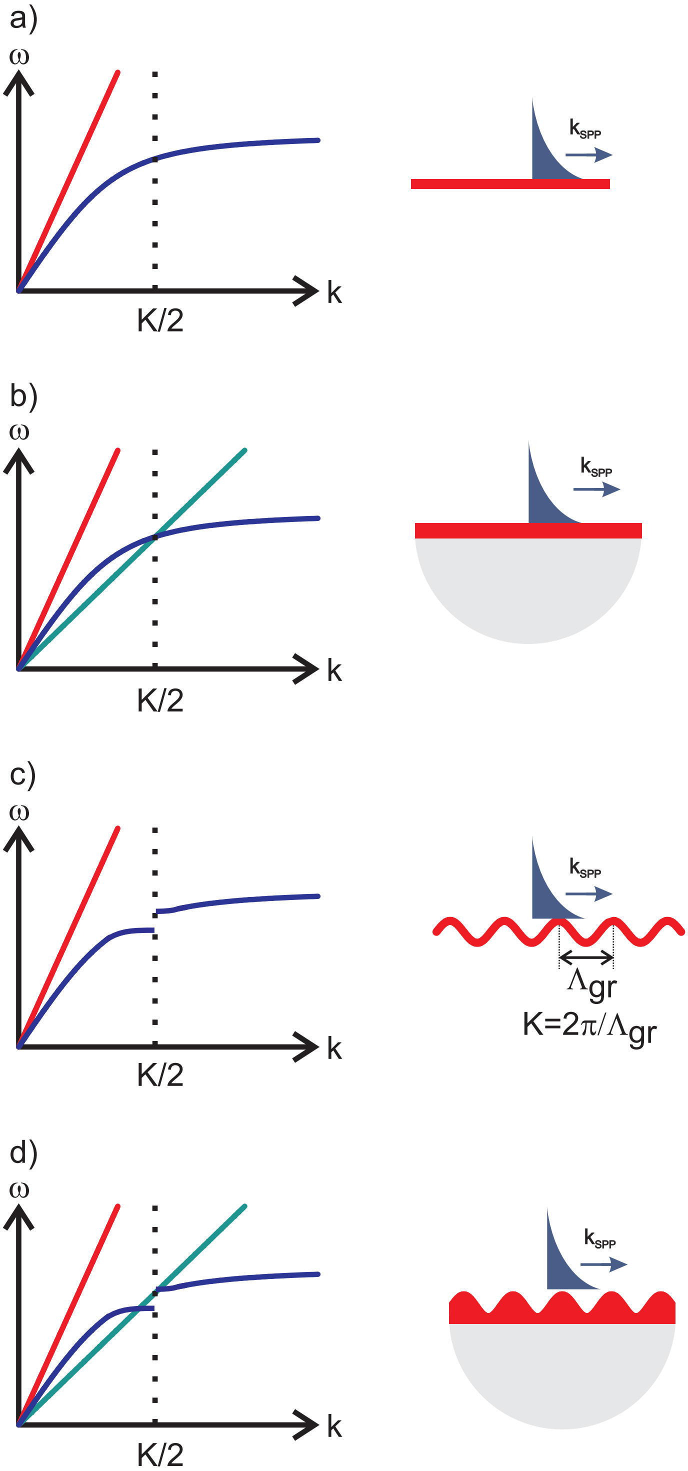

Figure 2.15: a) Dispersion curves of light line in air, SPP on flat metal surface. b) Dispersion curves of light line in air and prism, SPP on flat metal surface c) Dispersion curves of light line in air, SPP on a metallic uniform grating surfaceflat d) Dispersion curves of light line in air and prism, SPP on a metallic uniform grating

cavity formation in plasmonic structures in the literature.

It was announced that breaking the symetry in photonic band gap results in localized modes in the photonic band gap[13]. Then photonic cavity formation is demonstrated in the microwave and optical regimes in one, two and three dimensions[]. If we have a periodic multilayer dielectric as dicussed in the previous section before we observe a photonic band gap. However, we can break the symetry along the photonic crystal by adding an additional dielectric layer in this multilayer geometry. In this case a photonic cavity mode appears in the photonic band gap. The physical reason behind this localization is the constructive interference of the photons for that specific wavelength. The conditions and length of layers for the formation of this cavity is discussed in detail at [13].

Formation of plasmonic cavity can be also achieved by breaking the symetry in plasmonic band gap structures. The use of Bragg gratings for localization of propagating surface plasmons was suggested in 2007[15]. The cavity was composed of a thin film surface. Both right and left side of the thin film was surrounded by one dimensional Bragg gratings. The symetry breaking condition is satisfied using a thin film area in the Bragg grating region. The physical reason behind the localization of SPP is the constructive interference of SPP in the cavity region similar to photonic case. The phase change experienced by SPP after a roundtrip in cavity should be equal to reflected phase shifts on the Bragg gratings at the cavity. Then the cavity mode is achieved [15]. Similar approach was used to suggest plasmonic cavities for applications in quantum electro dynamics [16].

The physical reason behind the cavity formation for SPPs is controlling the phase changes experienced by SPPs. Removing grating ridges or using thin films surrounded by Bragg gratings support this condition. Using Moire patterns also enables localization of SPPs. Moire patterns having π shifts at its nodes acts as plamonic cavities[17]. Another way to control phase changes and demonstrate formation of plasmonic cavities is selectively coating the surface with a high index dielectric[18]. Here the effective indices seen by SPPs on dielectric coated and uncoated parts are different. This difference brings a phase shift and brings resonance. Whenever a resonance condition is met, SPPs at that specific wavelength constructively interfere and a cavity mode is achieved. Experimental demonstration of plasmonic cavities on Moire surfaces and biharmonic gratings have been achieved recently by our research group. The details of the experimental and numerical results for Moire patterns and biharmonic gratings will be discussed in Chapter 5.

Chapter 3

Fabrication and Measurment

3.1 Fabrication of Plasmonic Structures

This section provides the methods for fabrication of plasmonic gratings and their experimental characterization. Interference lithography is a widely used optical technology to produce periodic surfaces on large areas. It is a cornerstone technology for most Bragg grating devices. The physics behind this technology is the interference of two spatially coherent beams resulting in a standing wave pattern. The standing wave pattern consists of periodic fringes representing intensity maxima and minima. The two coherent plane waves overlapping in space and resultant standing waves are recorded on a photosensitive polymer. The periodicity is given by:

$$\Lambda = \frac{\lambda}{2sin(\theta)} \tag{3.1}$$

where Λ, λ and θ are periodicity of the grating, wavelength of the incoming light and angle between beams. In principal, a perfectly periodic pattern which is spatially coherent can be attained using this method. By spatially coherent we mean that the positions of all peaks can be known whenever position of one peak is known. The spatial coherence or in other words how the pattern is perfectly periodic is related to spatial and temporal coherence of the interfering beams. To support temporal coherence monochromatic light is needed. A laser

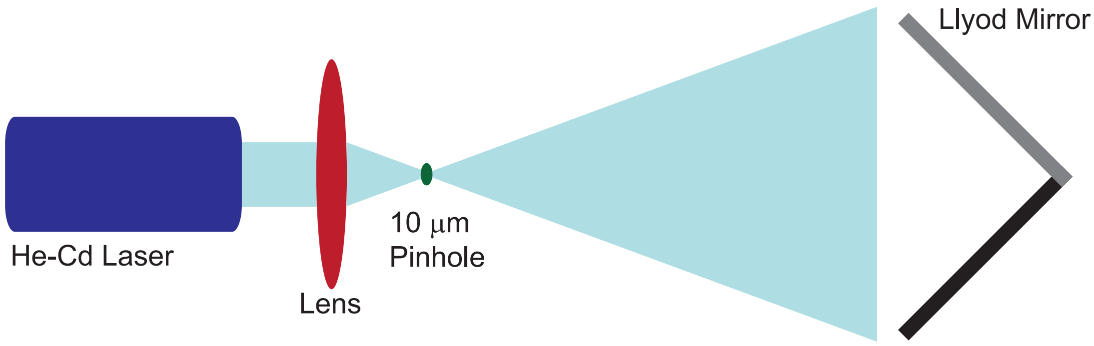

Figure 3.1: The interference setup used for fabrication of gratigs. The laser beam follows the lens-pinhole path. Expanded beam from pinhole reaches to Llyod mirror

can be used. The spatial coherence guarantees uniform wavefronts of plane waves. Using pinholes and spatial filters enables attaining uniform wavefronts. The Fig 3.1 illustrates the interference lithography we used for fabrication of gratings. A HeCd laser at 325 nm is used as the illumination source. First, the fused silica lens focuses the beam at its focal point, which is on order of mm's. The focused beam then goes through a 10 μm pinhole at the focal point of the lens. By using this pinhole we are able to eliminate nonuniformities and improve spatial coherence of the beam. The beam diverges after it passes through the pinhole and reaches to the Lloyd mirror as seen in Fig.3.1. The periodic pattern is recorded on the photosensitive polymer. The preparation of the sample can be summarized as: First a photosensitive polymer (S-1800) is spun on to a 100 um thick lamella. Then it is baked at 110 ^0C for one minute. After it is exposed at the interference setup, we put it in the developer to attain actual pattern physically. One of the problems with the interference lithography is that the interfering beams are not exact plane waves. Since the pinhole acts as a point source, the beams are actually spherical waves. This spherical behavior prevent obtaining perfectly periodic structures. However this effect is a very small. The main advantage of interference lithography is in making large area gratings, easily. The resolution is ideally limited by $\lambda/2$ that is 162.5 $nm = 325/2$ nm usually not available by optical lithography.

We use soft lithography to transfer the grating structures onto other substrates and materials. The transfer method enables us to examine the effect of

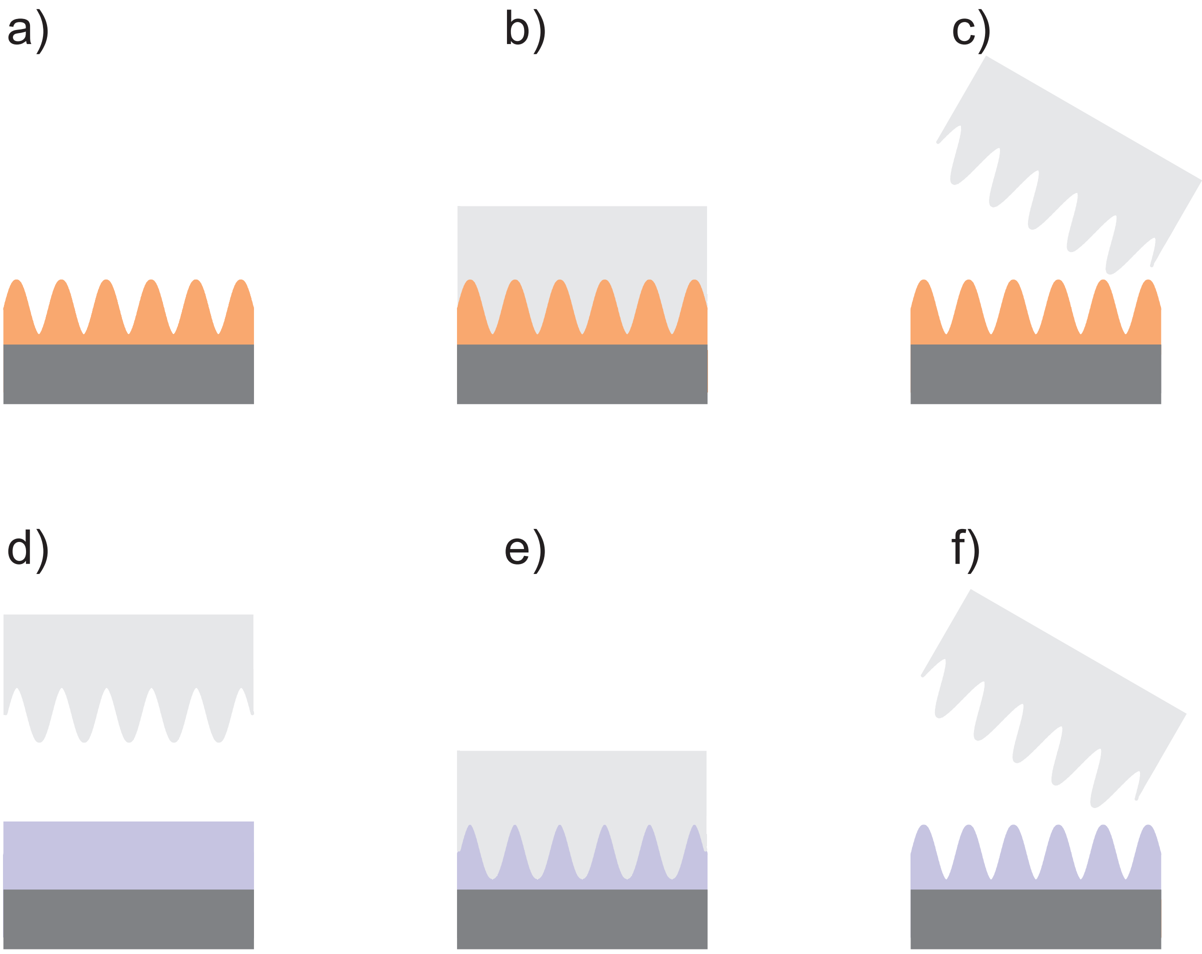

Figure 3.2: The steps of transferring a gratingin structure on photoresist on OG146

different thicknesses of metal films, dielectric films on the samples which have exactly the same geometry. Using this method, we transfer grating structures onto substrates which are resistive to chemicals such as acetone and these substrates are suitable for photolithography processes. We can photolithographly define patterns on these substrates, in our case leading to a cavity geometry, otherwise making patterns on the grating structure in the photoresist may destroy grating geometry. Soft lithography is a family of techniques for fabricating or replicating patterns. Elastomeric stamps, molds and comformable masks are used during soft lithography. The word soft comes from the usage of elastomeric materials. Elastomers which are conformable and easily peel of surfaces are the polymers which have elasticity property. The steps of the transferring process is shown in Fig. 3.2. The master grating structure on the sample is recorded on a photosensitive polymer (S-1800) which is spun on a 100 um thick lamella with interference lithography, described above. Typically, the periodicity is 300 nm and the size of the wafer is $2.4x3.2$ mm. Liquid PDMS (Sylgard 184, Dow Corning) is poured on top of the master grating which was cured for 2 hours at 75^0C. After the curing procedure, the elastomeric mold is removed from the grating surface. The low Young modulus of the PDMS makes the feature sizes. Due to thermal expansion during the curing process the periodicity of the grating is reduced by $1-2\%$. However, the uniformity is still preserved. The PDMS grating surface is then ready to be used as a stamp and transfer the pattern onto a photocurable prepolymer. The UV curable low viscosity prepolymer is spun on the lamella at 4300 rpm. The thickness of the polymer is around approximately 1 μm. The PDMS stamp is placed onto the polymer spun lamella without any pressure. The conformal contact on the surface leads to the attachment of PDMS to polymer coated surface. Due to capillary action, OG 146 fills the groves of the PDMS in seconds. The sample composing of PDMS and lamella is put under UV light for 2 minutes. The OG146 which was initially liquid is cured under UV light and solidifies. After the curing process, the PDMS stamps was mechanically peeled off. The solid polymer which has the pattern on the PDMS is left on the lamella. Thus, the transfer of the grating is successfully completed. A 50 nm-thick Ag film is evaporated on the samples to support metallic surfaces for excitation of SPPs.

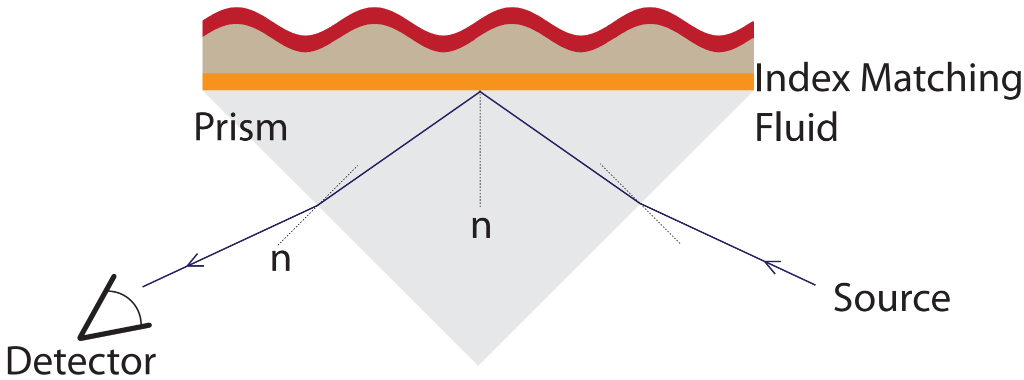

Figure 3.3: The schematic of optical characterization of plasmonic structures. SPP is excited by prism coupling technique.

3.2 Characterization of Plasmonic Structures

The characterization of samples was done by carrying out reflection measurements. Fig. 3.3 represents a simplified schema of our measurement setup.We used Kretchman geometry to overcome momentum mismatch and excite SPPs. A BK7 right angled prism is used in the experiment. An index matching fluid between the samples and the prism is used to minimize undesired reflections. The reflection measurements are done with a recogfigured variable angle spectroscopic ellipsometer W-VASE32. The ellipsometer is connected to a HS-190 monochromator to provide quasi monochromatic light from a white light source. The monochromator provides desired wavelengths for the system. There is an arc lamp filled with high pressure (above the athmospheric pressure) Xenon gas. When the lamp power is turned on, a high voltage pulse is sent through the lamp causing an arc to start the lamp. Lower DC voltage maintains to support arc. The lamp is mounted in the monochromator lamp housing. The focal length of the monochramotor is 160 mm and effective aperture ratio is f/4.5. The spectral range of the monochromator is 250-1700 nm. We have typically used the 500-750 nm regime. The light is coupled from the exit of monochromator to a fiber optic cable, where the beam is collimated and polarized. The fiber optic cable enters the input unit where additional polarization states are added. Here we do not list details of the ellipsometer such as autoretarders, analyzer etc. which are also used for thin film thickness and refractive index measuresments. Since

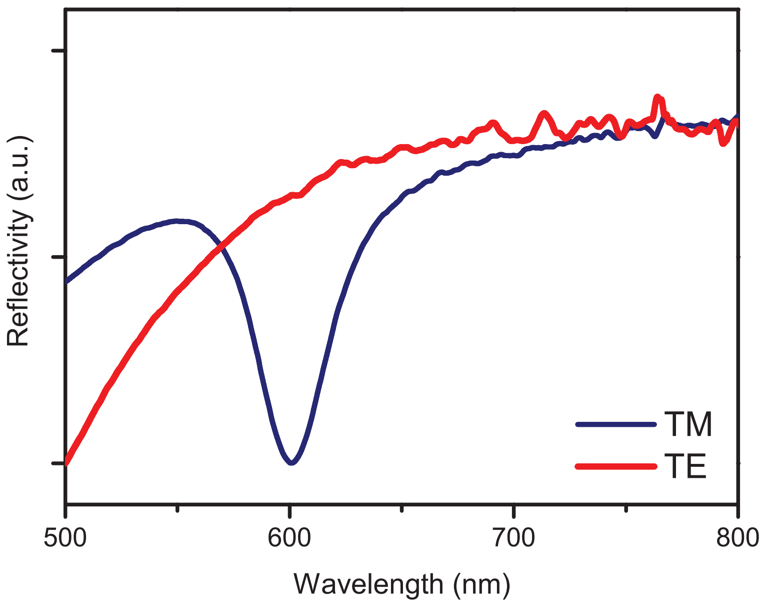

Figure 3.4: The reflection spectra of flat Ag film taken in the Kretchmann geometry for TE and TM modes. The minima in the TM case stand for SPP excitation at metal-air interface

we perform only reflection measurements, important parts of the ellipsometer for our experiments are limited to monochromators and detectors. The samples are aligned in the x, y, z directions using a sample stage. The detector is placed at the end of the detector unit, converts light energy into voltage. The goniometer base together with the sample stage and input unit is used to precisely control the angles of incidence with a precision of 0.001^0 degrees. An experimental data is shown from our measurements in Fig. 3.4. We look the SPP coupling on a flat metal surface in the Krecthman geometry. We have carried measurement for TE and TM modes seperately. The metallic film thickness is 50 nm. The results are shown in Fig. 3.4. We observe an absorbtion peak around 600 nm at an angle of incidence 42^0 indicating SPP excitation. For TE case there is no resonance absorbtion.

Chapter 4

1D Grating Based Plasmonic Cavities

In this chapter, a comparative study on grating based plasmonic band gap cavities is presented. Numerically, we calculate the quality factors of the cavities based on three types of grating surfaces; uniform, biharmonic and Moirè surfaces. We show that for biharmonic band gap cavities, the radiation loss can be suppressed by removing the additional grating component in the cavity region. Furthermore, due to gradual change of the surface profile around the cavity region, Moirè type surfaces support cavity modes with higher quality factors. Experimentally, we demonstrate the existence of plasmonic cavities based on uniform gratings. Effective index perturbation and cavity geometries are obtained by additional dielectric loading. A quality factor of 85 is obtained from the measured band structure of the cavity

4.1 Introduction

It is well known that metallic periodic structures exhibit modified transmission and reflection spectra owing to the interaction of the propagating SPPs with the periodicity. Many features of these SPPs that are excited on periodic metallic surfaces are extensively studied. Surface enhanced Raman scattering and photoluminescence signals have already been observed on such structures [19]. In contrast to localized SPPs on nanoparticles, propagating SPPs on periodic surfaces are also being studied in nanolithography and nanophotonic applications [20]. Recently, plasmonic cavities that use Bragg reflectors and selective dielectric loading have been under investigation[16][18][15]. In addition to uniform gratings, biharmonic gratings and Moirè surfaces can be used to construct cavity structures. Such cavities can localize plasmons and can lead to small group velocities around the band edges. While these structures all localize the plasmons, they exhibit different characteristics due to the difference in their design and the mechanism of confinement.

On the other hand, metallic loss at visible wavelengths is a serious problem that hinders the use of plasmons for applications that require long propagation lengths and plasmonic lifetimes. Due to this same reason, current cavities with relatively low quality factors need to be improved to meet expectations. Large quality factors for SPPs, localized in cavities, are crucial for many applications. A cavity designed for localization of SPPs with high quality factors can be used to selectively enhance and suppress spontaneous emission rates of emitters and may provide an ideal platform for cavity quantum electrodynamics (QED). SPP cavities that are expected to work in the strong coupling regime with large Purcell factor enhancements have been suggested. Quality factors as high as 1000 have been proposed [16]. Bragg mirrors used in so many photonic structures have been suggested for simple confinement in one dimension and have been shown to exhibit enhanced Purcell factors for applications in cavity QED. Such mirrors have also been employed for SPP localization and characterized with scanning near field optical microscopy to map the electric field distribution in and out of the cavity. Results confirm the cavity formation and localization of the SPP modes. Alternatively, using double exposure interference lithography, biharmonic gratings were employed to localize SPPs. The quality factor of the demonstrated plasmonic cavity was 37 due to metallic and scattering losses in the cavity [18]. Very recently, Moirè surfaces have been demonstrated to support SPP localization at the nodes of a metallic Moirè surface. Smooth variation of the surface

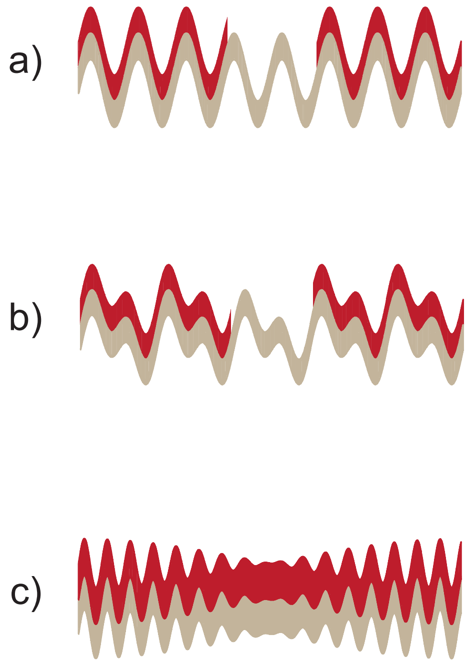

Figure 4.1: Surface profile of a) uniform, b) biharmonic and c) Moirè gratings. Note the selectively coated dielectric (red line) on the biharmonic and uniform gratings and the cavity region. Localization takes places around the node of the Moirè surface.

relief amplitude in these structures reduces radiative losses leading to relatively high quality factors (Q=103) [17]. The increased quality factor is promising and suggests further study. Experimentally, we demonstrate plasmonic cavity formation on uniform metallic gratings, which consists of a single periodic surface as shown in Fig. 4.1a. Because surface plasmons are sensitive to the effective index of the medium, localization on uniform gratings have been achieved by selectively coating the metallic surface with silicon. To couple light to the surface plasmons, Kretchman configuration is used to overcome the momentum mismatch between surface plasmons and incoming light. The band gap is provided by the uniform metallic grating while the prism allows the SPP excitation [14]. The characteristics of the Q factor of plasmonic cavities on uniform, biharmonic gratings and Moirè surfaces are studied numerically. The biharmonic grating, as shown in Fig.4.1b, consists of two periodic surfaces with periodicites such that $\Lambda_1 = 2\Lambda_2$.

SPP excitation and band gap formation are achieved by using the grating components. The plasmonic cavity mode is obtained through selective loading of the metallic surface. Numerical results indicate that as the amplitude of the larger component is increased the quality factor decreases. The *Moirè* surface which is a superposition of two periodic surfaces with slightly different periodicities as shown in 4.1c also support plasmonic cavities. The phase shift at the nodes of the surface leads to localization of the SPPs. The slowly varying grating amplitude around the cavities results in higher quality factors. Different Moirè surfaces are studied to compare their respective quality factors.

4.2 Fabrication and Experiment

Fabrication of a uniform grating was achieved with an interference lithography setup as we discussed in Chapter 3. We, first spin a photosensitive polymer (S1800) on 170 μm thick microscope lamella and bake the photosensitive polymer at $110^0 C$ for 1 minute. A 325 nm He-Cd laser was used to record periodic structures on the photosensitive polymer using Lloyd's mirror configuration. Once the structures were developed, they were transferred onto a photocurable polymer (OG146) by the nanoimprint technique. Biharmonic gratings and Moirè surfaces require double exposure of the periods. A 50 nm thick silver film was evaporated on the OG146 polymer to support the surface plasmons. The lamellae was then mounted on the base of the prism with the metallic side up and index matching fluid was used between the prism and the lamallae. The BK7 prism allows incoming photons to couple to the plasmons. The coupling condition is satisfied at a specific wavelength and angle of incidence. This condition is given by

$$k_{SPP} = n_{EFF} k_0 = n_p k_0 sin(\theta) \tag{4.1}$$

where k_{spp} and n_{eff} are the wavenumber and the effective index of the SPPs. k_0, θ and n_p are the free space wavenumber of incident photon, angle of incidence and refractive index of the prism, respectively. The dispersion curves of SPPs are constructed by measuring the coupling wavelength and angle. We used a spectroscopic ellipsometer (VWASE32) for precise reflectivity measurements. The

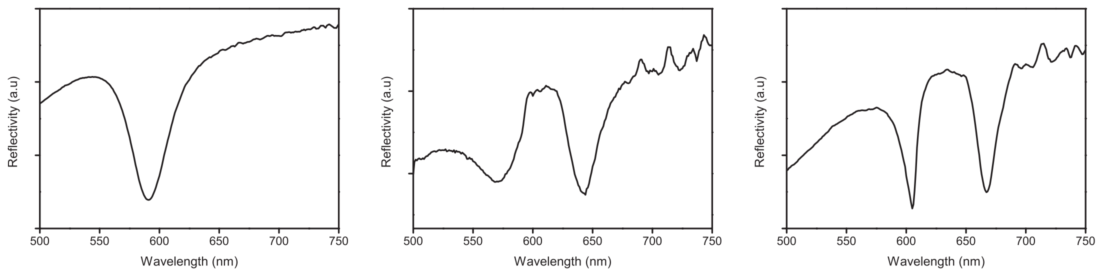

Figure 4.2: Reflectivity spectra of a) flat metallic surface, b) uniform metallic grating, c) uniform metallic grating coated with 10 nm of silicon.

reflection measurements at different angles of incidences result in two dimensional reflectivity maps. In order to construct the band structure with high resolution, we scanned the 500-750 nm wavelength range at various angles of incidence with a resolution of 0.2 apart.

4.3 Uniform Plasmonic Band Gap Cavities

In Fig.4.2, wavelength dependent reflection spectra of three different structures are shown with the corresponding experimental configurations. Fig. 4.2a shows the reflection spectra of the TM polarized light from a flat metal surface. As expected, we observed the plasmon resonance at the wavelength of 580 nm. However, periodic structure on the surface modifies the dispersion relation. This modification is manifested in the reflection spectrum of a uniform grating and is shown in Fig. 4.2b. Propagating SPPs interact with the grooves of the grating and are backscattered. This leads to the formation of standing SPP waves on the uniform grating. Symmetry suggests the presence of two standing waves, labeled λ_- and λ_+, with two different energies. One localizes on the peaks and the other on the troughs of the periodic structure [11]. A band gap is opened up due to the energy difference between λ_- and λ_- modes. The gap is located approximately at 600 nm with the band edges observed at 560 and 635 nm. The width of the band is 23 nm. When the uniform metallic grating is coated with a thin layer of silicon, the effective index experienced by the SPP mode increases, and opens up the band gap. The reflectivity spectra of the uniform metallic grating coated with

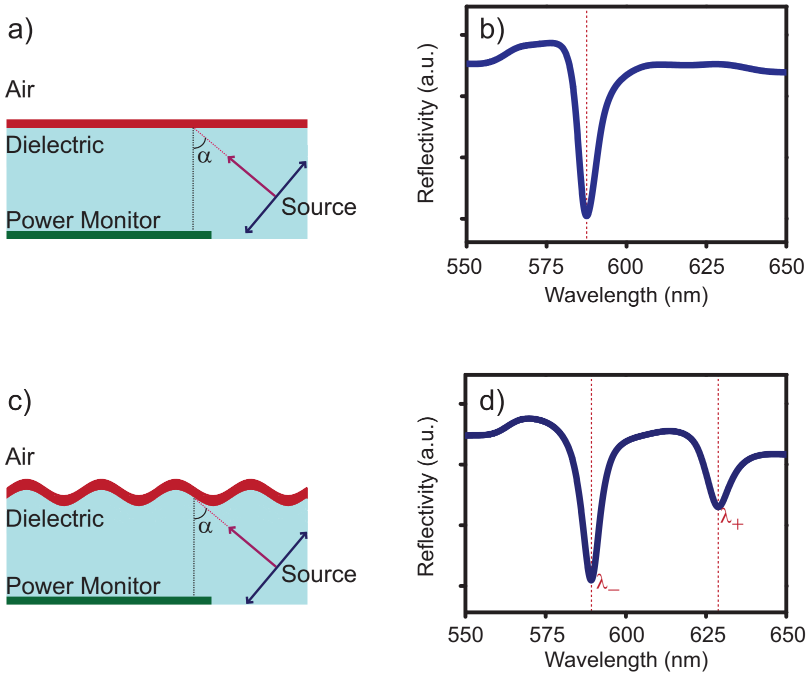

Figure 4.3: Schematic representation of simulated structure for a) flat metallic surface, b) uniform metallic grating. FDTD simulation results of reflectivity measurements for c) flat metallic surface, d) uniform metallic grating

10 nm of silicon is shown in Fig. 24.2c. Red shift of the spectrum and opening up of the band gap are clearly observed. The red shift is due to the effective index change, induced by silicon. The widening of the band gap comes from different confinement properties of λ_- and λ_+ modes on the grating surfaces. The low frequency mode is confined closer to the surface of the samples while the higher frequency component has a longer evanescent tail.

The different confinement behavior of λ_- and λ_+ can be understood better with the numerical investigations. We have employed the Lumerical software program to examine the plasmonic characteristics of the structures. The program uses finite difference time domain (FDTD) technique to obtain optical characteristics of the structure. The details of the computational method is given in Appendix A. We have used nonuniform mesh around metal-dielectric interfaces, $\lambda/10$ mesh size is used for uniformly meshed parts of the simulation area and 2.0 nm mesh size is used for the nonuniform meshing area. We first studied the surface plasmon excitation on a flat metal surface. The simulation geometry is

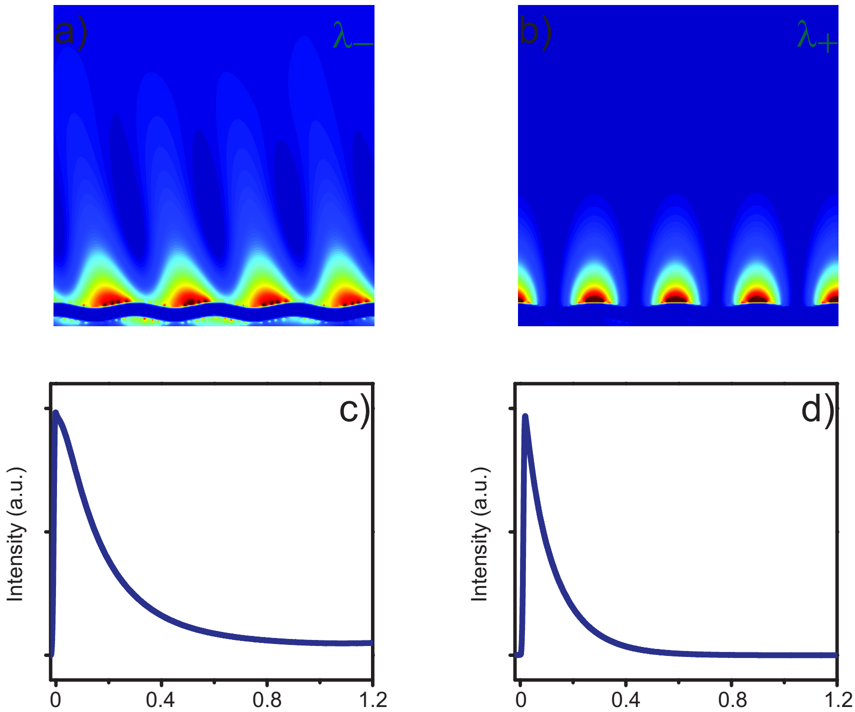

Figure 4.4: Electric field distributions of surface plasmon polariton at band edges. a) Higher energy configuration for λ_- b) Lower energy configuration for λ_+ Electric field intensities at the metal-air interface c) Higher energy configuration for λ_- d) Lower energy configuration for λ_+

shown in Fig.4.3a and b. We launch a Gaussian wave from a dielectric medium and look at the power of the reflected light from metal-air interface. The power of reflected light is read through the monitor in the simulation domain. The refractive index of the dielectric medium is 1.56 and the value of dielectric function of the metal is taken from Palik [21]. The metal thickness is 50 nm. The reflectivity maps of the flat metal surface is studied for both TE and TM polarization states. In Fig.4.3c the reflectivity maps taken at $\theta = 45$ are shown. The SPP excitation is seen for only TM polarized case, as expected. Next, we have inserted a uniform grating with a periodicity of 290 nm and amplitude of 20 nm similar to the experiment we described above. The geometry in the simulation is shown in Fig.4.3b. The reflectivity spectra for uniform grating is shown in Fig.4.3 The $\lambda_- = 589$ nm and $\lambda_+ = 628$ nm are labelled with red lines. Then we have studied the electric field configurations of λ_- and λ_+. Fig.4.4a and Fig.4.4b shows the electric field distributions of λ_- and λ_+ respectively. λ_+ localizes on the peaks

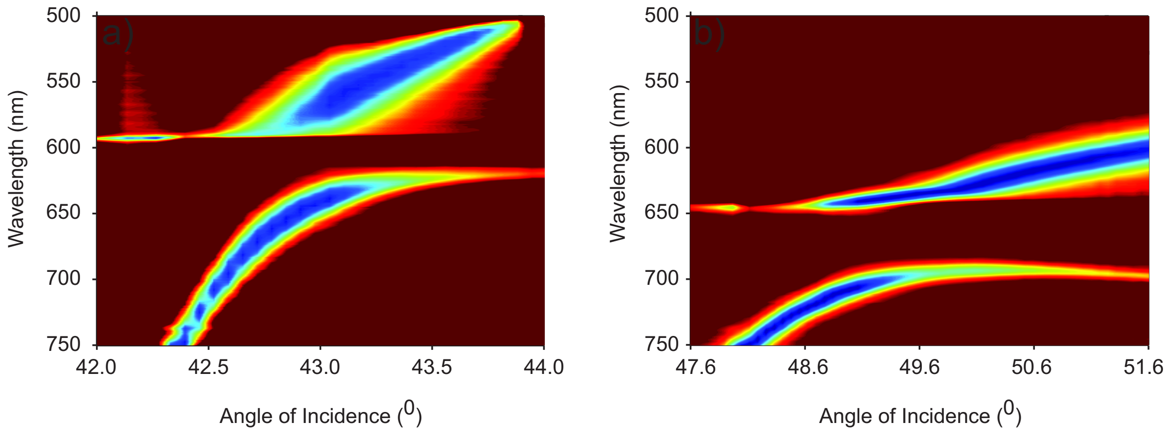

Figure 4.5: Dispersion maps of uniform metallic gratings in the Kretchman configuration without Si coating (a) and with 20 nm Si coating (b)

and λ_- localizes on trougs. 4.4c-d shows the confinement behavior of λ_- and λ_+. λ_+ shows a more confined behavior than λ_-. So λ_+ becomes more sensitive to surface properties. Then coating the surface with Si increases the energy difference between λ_- and λ_+ resulting in widening the band gap width while the central wavelentgth of the band gap shifts slightly to longer wavelengths. This property of band edges allows one to effectively tune the SPP band gap width and position by adjusting the thickness of the dielectric layer. A series of experiments with uniform metallic gratings coated with different silicon thickness were performed and the reflectivity of the samples were measured. The position and width of the band gap were determined. Effective index of the structure was calculated from the center of the band gap, since $n_{EFF} = n_p sin(\theta)$.

Experimentally, we construct the band structure for both the uniform metallic grating and that of the dielectric loaded grating in Fig. 4.5. The set of measurements were interpolated using linear interpolation. Both the shift of the band gap in terms of angle of incidence as well as widening of the band gap is observed. Fig. 4.5a is the experimental band structure of a uniform metallic grating in the Kretchman geometry. The band gap is centered at 603.0 nm with a width of 23.0 nm. The coupling angle indicating varies between 42.0^0 and 44.0^0, the corresponding effective index n_{EFF} is 1.03. The result for 20.0 nm silicon loaded uniform metallic grating is given in Fig4.5b. The center of the band gap is shifted to 668.0 nm and the width is increased to 36.0 nm. The coupling angles

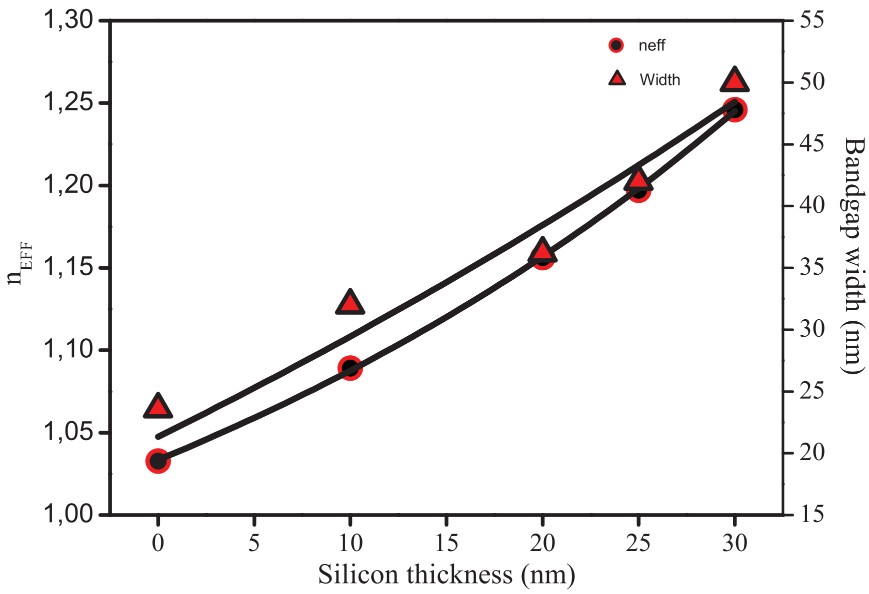

Figure 4.6: Effective index and width of the band gap of a uniform metallic grating as a function of silicon loading

also change to satisfy the resonance condition. n_{EFF} becomes 1.15 at 49.6^0 for this case.

The increase in n_{EFF} causes significant changes in the coupling conditions. Larger angle of incidences for incoming photons are needed to compensate for the momentum mismatch in the silicon loaded case. We summarize the results in Fig. 4.6. The effective index of SPPs can be seen to tune from n_{EFF} =1.03 to n_{EFF} =1.24 due to silicon loading and the width of band gap is observed to change from 23.0 nm to 50.0 nm.

Band gap occurs due to destructive interference between forward and backward propagating SPPs in the uniform metallic grating. Constructive interference at a specific wavelength in the band gap can be attained by tuning the relative phases of the propagating waves. Local perturbation of the effective index can lead to these phase changes and enable a localized state in the band gap, called the cavity mode. Having already demonstrated the ability to control the effective index, we design a SPP cavity for the wavelengths in the band gap, using the

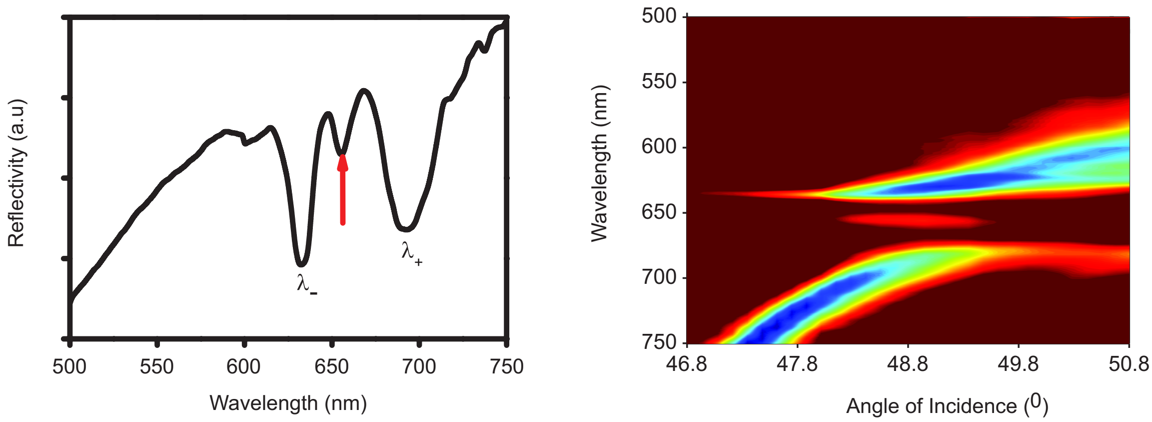

Figure 4.7: Reflectivity spectra a) and band structure b) of uniform metallic grating with the cavity structure. Note the cavity state in the band gap localized due to selective loading of uniform metallic grating

resonance condition:

$$L\Delta = (2m+1)\frac{\lambda}{4} \tag{4.2}$$

where L is the length of the cavity, Δn is the effective index difference and λ the central wavelength in the band gap. We start the fabrication of the cavity by photolithographically defining the cavity geometry on the uniform metallic grating. The sample has a number of cavities with the same geometry separated by 10 micrometers in an area of $10 \times 10mm^2$. A silicon layer with a nominal thickness of 18.0 nm was deposited on the surface outside the cavity regions. The effective refractive index of SPPs for silicon-coated and uncoated regions of the metallic grating are determined to be $n_0 = 1.03$ and $n_1 = 1.14$ respectively. High resolution reflectivity spectra of these samples were measured as a function of the angle of incidence. The results are shown in Fig.4.7. To clarify cavity formation, we constructed band diagrams of uniform gratings with the cavity. The observed band structure without the cavity is modified with the inclusion of a cavity state in the middle of the band gap, Fig.4.7b. This is the result of an additional absorption peak observed in the reflection spectrum of the cavity, Fig.4.7a. We observe the cavity mode at 655.0 nm for 4.40 m cavity length when m=1. The Q factor is calculated as 85 while the full-width-at-half-maximum of the absorption peak is 7.7 nm. We have employed the Lumerical software package to examine the effect of the cavity structure on the Q factor, as well as on plasmonic bandgap width and effective index. The simulation geometry is shown in Fig.4.8. The

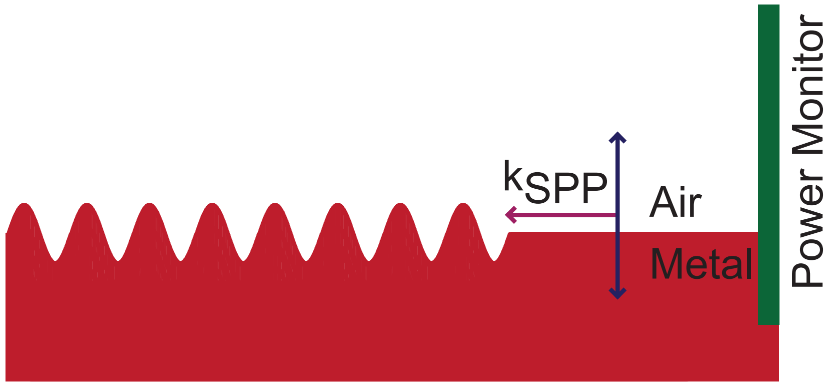

Figure 4.8: Schematic representation of simulation geometry

Fig. 4.9 represents the interface of the program where the simulation domain is seen. The Fig. 4.10 represents the source properties dialog box. The surface plasmon polariton mode is excited at the metal-air interface which propagates through the structure of interest. The reflection spectrum along the excitation axis is attained from FFT analysis. We have studied gratings with a periodicity of 290.0 nm with amplitudes changing from 5 nm to 50 nm. The propagation of SPP are forbidden for the wavelengths around $\lambda = 580nm$. The width of the band gap is increased from 3.5 nm to 70.0 nm by changing the amplitude of the grating. As the amplitude increases SPP are scattered more effective and the width of the band gap increases. This is analagous to the dependence of the photonic band gap on the refractive index difference of dielectric layers, Δn. We have used the grating with a modulation depth of 20.0 nm since the corresponding bandgap width is similar to the experimental case. Varying the thickness of the evaporated Si on the grating structure, we studied the effective index and the band gap width. The SPP effective mode index increased from 1.0356 to 1.1110 as the Si thickness was increased to 18 nm. Similarly, the band gap width is also increased from 18.7 nm to 38.1 nm. This behavior is summarized in Fig.4.12 and consistent with the experimental results shown in Fig.4.6. Selectively loaded cavity geometry on the grating structure was studied under resonance as introduced in Eq.4.2. The expected minima in the band gap region, where normally no SPP excitation is allowed, was observed at 652.0 nm for a cavity length of 2.4 μm with a dielectric thickness of 14.0 nm for m=0. The small difference between the expected cavity length of 2.2 μm and the observed

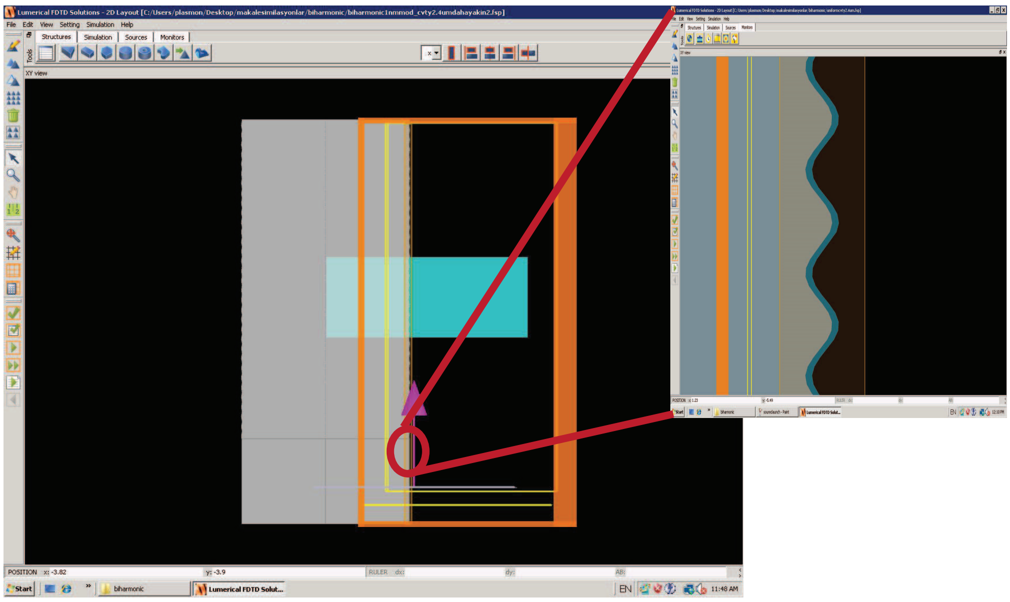

Figure 4.9: The interface of the simulation domain

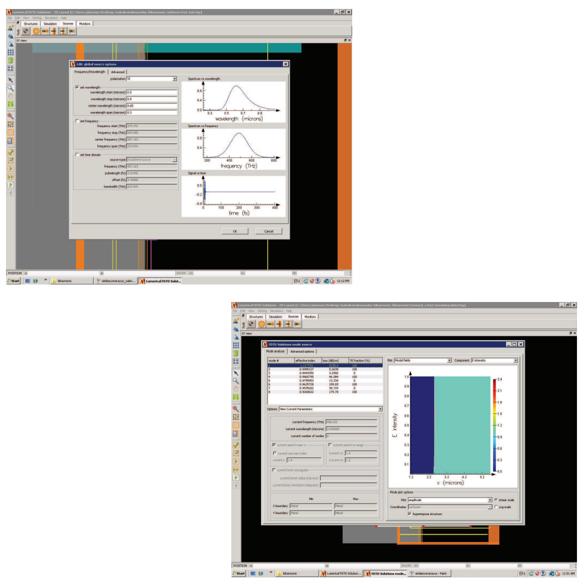

Figure 4.10: The interface of the source properties dialog box

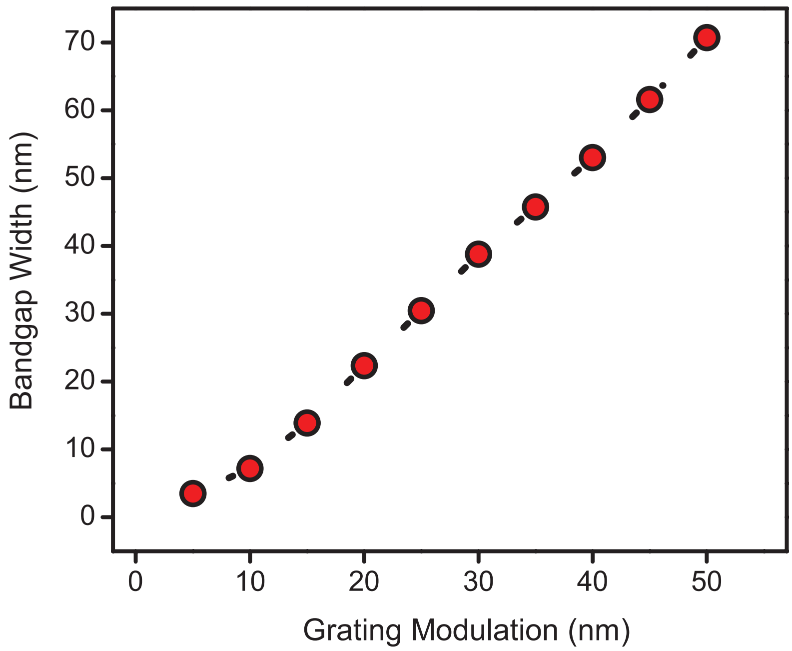

Figure 4.11: FDTD simulation results for the width of the band gap as a function of grating amplitude

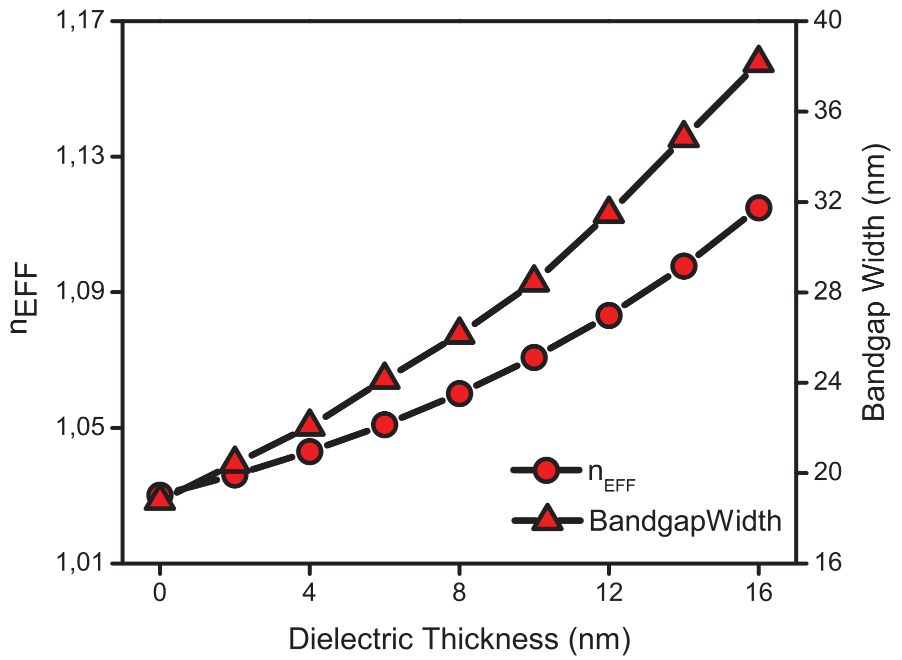

Figure 4.12: FDTD simulation results for the n_{EFF} and the width of the band gap as a function of dielectric loading on the surface

a)

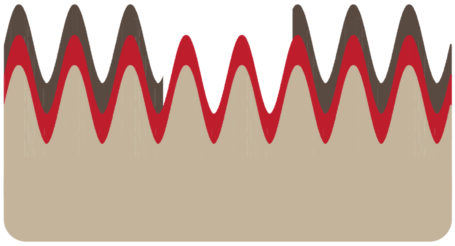

b)

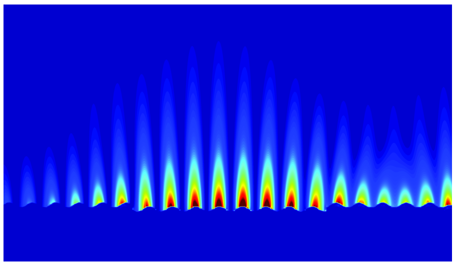

Figure 4.13: a)Schematic reprasantation of the plasmonic cavity structure on uniform grating. b) FDTD simulation of the electric field distribution in a cavity illuminated with the cavity mode

cavity length of 2.4 μm, is due to differences between effective indices of SPPs on corrugated and flat surfaces, since we calculate the effective indices for a flat surface but measure it on the cavity geometry of the grating surface. The cavity geometry and field profile of the cavity mode is illustrated in Fig.4.13a and Fig.4.13b respectively. The localization of the field inside the cavity can be clearly seen. The electric field distribution is slightly asymmetric since the excitation was done from the side of the structure. We also studied the effect of metal thickness on the quality factor of the cavity. The SPP excitation is the same as above. The quality factor changes from 40 to 70 as the thickness of metal layer changes from 40 nm to 1 μm. This behavior can be understood through the radiation losses through the dielectric layer. While the thickness is small SPP reradiates into the dielectric layer as photons. The quality factor converges to its maximum value after 80 nm of metal thickness since this thickness limits the radiation of SPP into dielectric layer.

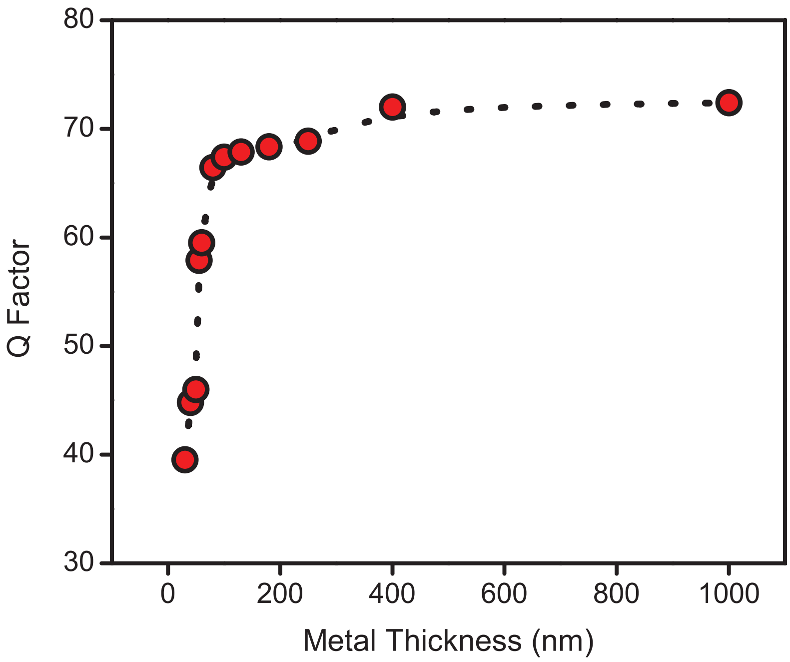

Figure 4.14: FDTD simulation results for the quality factor of the plasmonic cavity on uniform metallic grating as a function of thickness of metallic layer

4.4 Biharmonic Plasmonic Band Gap Cavities

Biharmonic gratings are formed by superimposing two uniform gratings with different periodicities. The grating periods are chosen such that $\Lambda_2 = 2\Lambda_1$,where Λ_2 is used to couple SPP, Λ_1 is used to form plasmonic band gaps. The schematic representation of a biharmonic grating is shown in Fig.4.15. The biharmonic geometry can also be recorded on a photoresist using interference lithography. After the grating is developed, it is transferred onto a polymer (OG146) and a 50.0 nm metallic thin film is evaporated on the surface to create the metallic surface. These structures have been shown to support plasmonic band gaps and plasmonic cavities through selectively loading of dielectrics, by our research group. There, we have then argued that the grating component which has larger periodicity can lead to radiative losses causing a low quality factor. Our analysis suggested that reducing the grating amplitude can lead to an increase in the quality factor. In order to verify these proposals, we have studied the properties of the biharmonic gratings with FDTD simulations using Lumerical software. We construct a biharmonic grating with periodicities $\lambda_2 = 580$ nm with a modulation

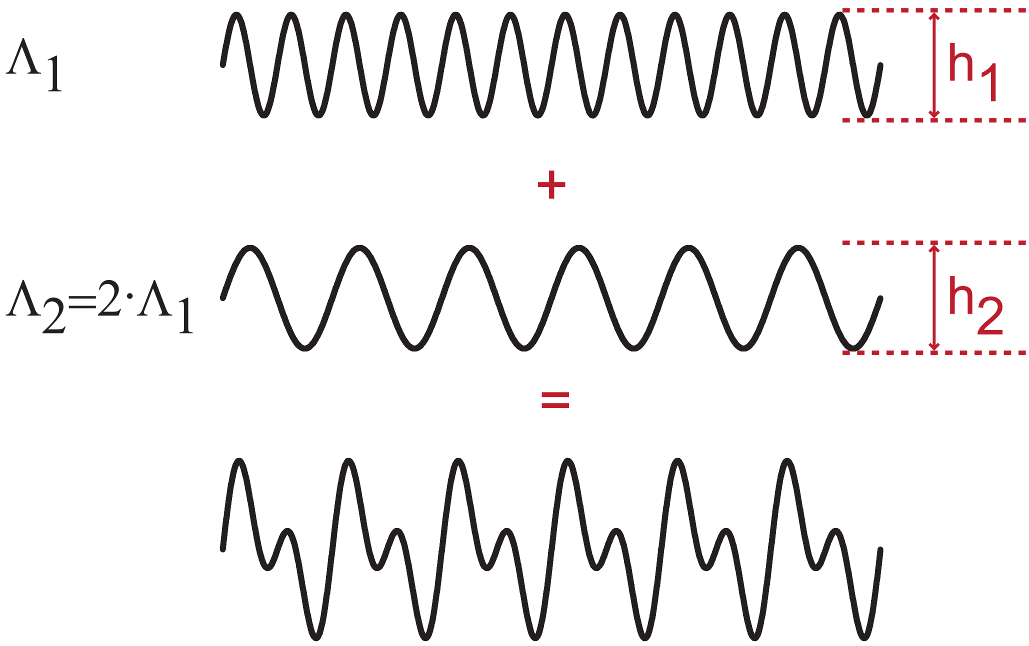

Figure 4.15: Schematic representation of biharmonic grating

depth of $h_2 = 20.0$ nm, $\lambda_1 = 290$ nm and with a modulation depth of $h_1 = 20.0$ nm, selectively loading the surface with a dielectric with a refractive index of 2.4. The structure under study is depicted in Fig.4.16a. A clear cavity mode in the band gap and the associated electric field intensity in the cavity is shown in Fig.4.16b. The confinement characteristics of the biharmonic cavity are summarized in Fig.4.16. In addition to the field distribution in Fig.4.16b, we study the change of the Q factor with the amplitude of the larger period, h_2. The results are shown in Fig.4.17. As we increase the amplitude of this component from 0.0 nm to 40.0 nm, we observe a decrease in the quality factor from 70.0 to 40.0. This is most likely due to out-of-plane radiative losses caused by this additional grating component. This idea is supported by the quality factors observed on uniform gratings reported above.

4.5 Moirè Surfaces

Moirè surfaces are geometries that consist of two gratings with slightly different periods as shown in Fig.4.18. The Moire surface can also be expressed as a

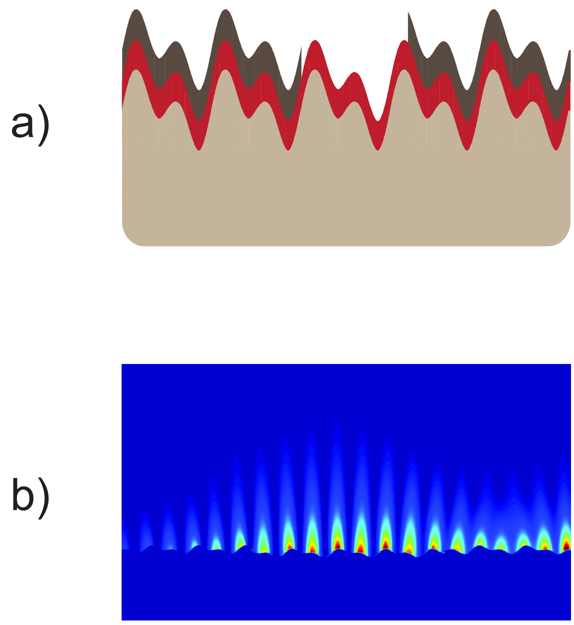

Figure 4.16: a)Schematic represantation of the plasmonic cavity structure on a biharmonic grating. b) FDTD simulation of the electric field distribution in a cavity illuminated with the cavity mode.

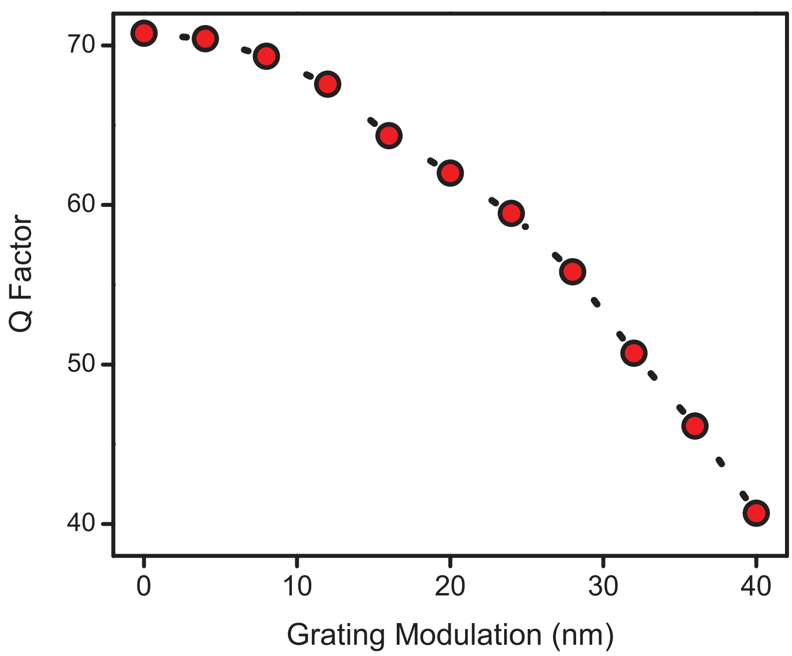

Figure 4.17: FDTD simulation result for dependence of quality factor (Q factor) on grating amplitude h_2

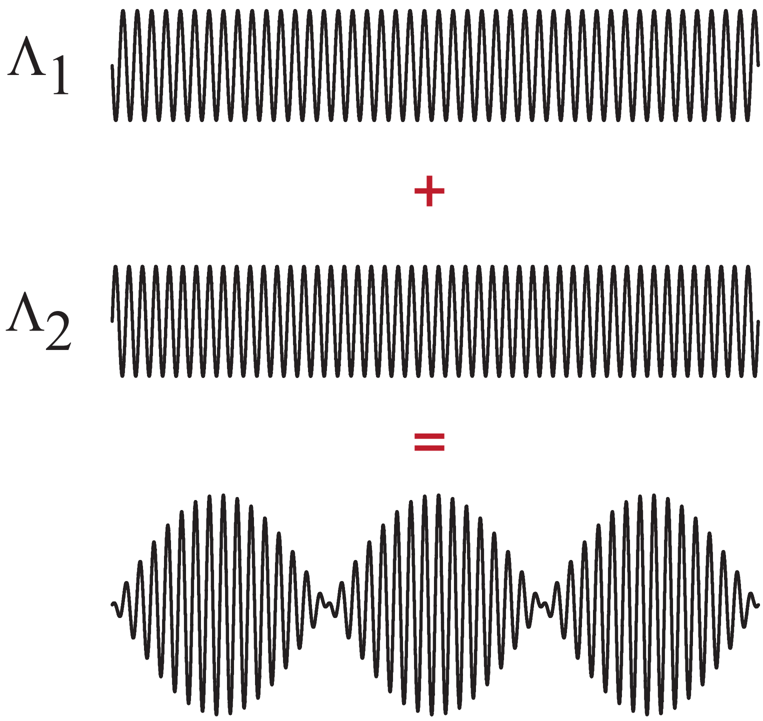

Figure 4.18: The Moirè pattern formation

superposition of a uniform grating and an envelope function which generates a superperiodicity, D, which is representative of the surface profile. The final Moire surface can be represented by:

$$S(x) = cos(Gx)sin(gx) \tag{4.3}$$

where $g = \frac{2\pi}{d} = 2\pi\frac{\Lambda_1+\Lambda_2}{\Lambda_1\Lambda_2}$,$G = \frac{2\pi}{2D} = \frac{\Lambda_1-\Lambda_2}{\Lambda_2\Lambda_1}$, d and D are the uniform periodicity and the periodicity of the superstructure (half the periodicity of the envelope function). It has been shown that Moire surfaces can also support plasmonic cavities. There are π phase shifts at the nodes of the Moire surfaces that lead to SPP localization. Experimentally, we have shown that these surfaces support slow surface plasmons [17]. Here, we show the results of the simulation of the cavity state on the Moire surfaces. A Moire surface consisting of a grating period of Λ_1 = 317.2 nm with a modulation depth of 10.0 nm and a grating period of Λ_2 = 325.0 nm was chosen. We study the effect of surface profile on the Q factor interms of half of the superperidiocity, D. We observe a cavity mode at 656 nm with a quality factor of 112 on a Moire surface with d = 321 nm and D = 13.6 μ. The electric field distribution can be seen in Fig.4.19b. In this

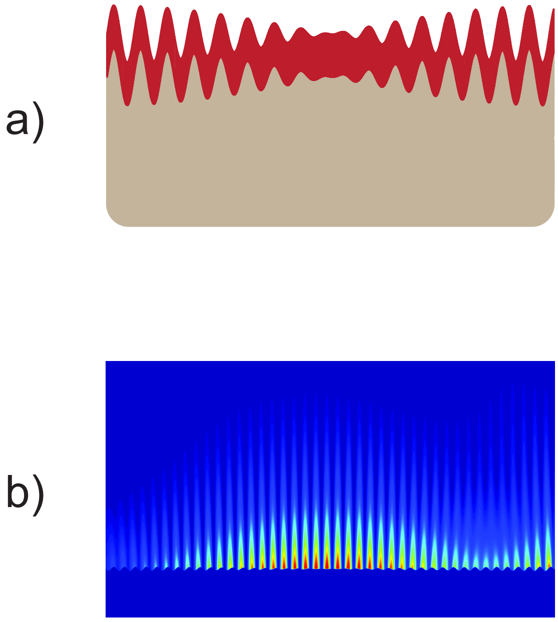

Figure 4.19: a)Schematic representation of the plasmonic cavity structure on Moirè surface b) FDTD simulation of the electric field distribution in a cavity illuminated with the cavity mode.

regime, cavities are weakly coupled and slow variation of the grating amplitude leads to high quality factors. As we decrease the superperiodicity, the coupling of cavities increases and the quality factor decreases. The cavity Q factor observed on a Moire surface is relatively high when compared with a cavity on a uniform grating. It is also consistent with the Q factors calculated for the biharmonic grating cavities when the amplitude of the second component in the biharmonic grating is small. High Q-factor performance of the Moire surface is consistent with our assertion that removing the second component or using a slowly varying envelope function reduces out-of-plane scattering and leads to higher Q-factors.

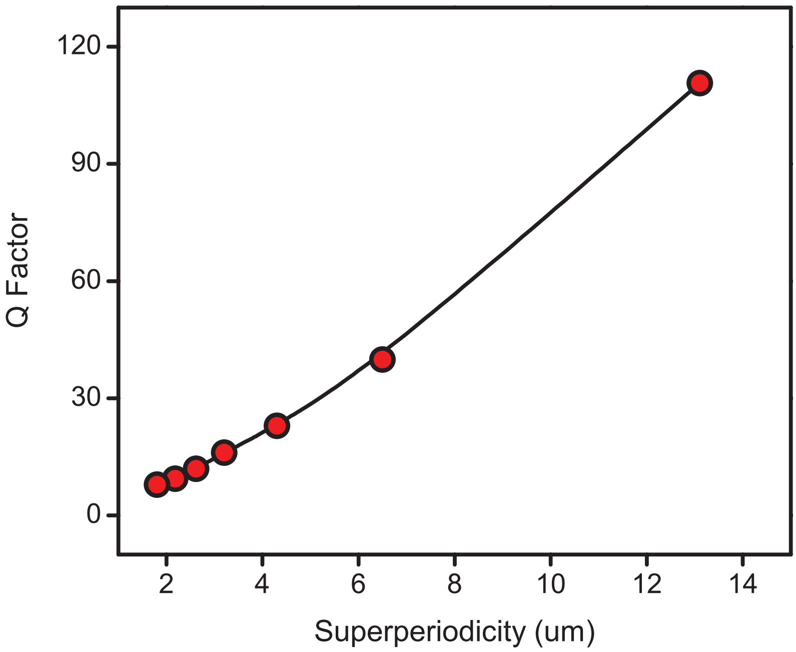

Figure 4.20: FDTD simulation result for dependence of Q on superperiodicity D

Chapter 5

Conclusions and Future Work

In this chapther, we report the preliminary results of our study on two-dimensional plasmonic crystals. We will remark the conclusions we have arrived and make a plan for future work. Two dimensional metallic gratings were fabricated and excited the SPP resonances in the Kretchman configuration. The goal of the study was to show theexistence of plasmonic band gaps along the symetry axes of 2D dimensional plasmonic crystal and propose cavity geometries for the structures.

5.1 Introduction

In Section 4.1, the modified transmission and reflection spectra of propagating SPPs with the 1D crystals was discussed. In particular, to get a maximum effect for surface enhancement of Raman scattering and photoluminescence signals a full plasmonic band gap is required [22]. In this regard, experimentally and theoretically, full plasmonic band gaps for two dimensional gratings are shown[23][22][24]. Recently, in plasmonic crystals composed of triangular lattices composed of gold bumps and the effect of surface geometry are studied[25]. Numerically,dependence of central wavelength and width of the band gap on the structural properties of the plasmonic crystal composed of cylinders is studied. Experimental enhancement

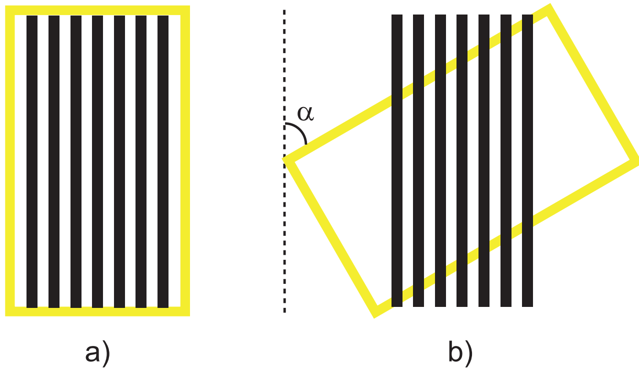

Figure 5.1: a)The configuration of the sample for the first exposure b)The configuration for the second exposure. Black and white regions are schematic representation of interference pattern

in the florescence of methylmethacrylate on two dimensinal plasmonic structures is shown. As we discussed in Section 4.1 metallic loss at visible wavelengths is a serious problem that hinders the use of plasmons for applications that require long propagation lengths and plasmonic lifetimes. The plasmonic cavities seem to overcome this problem. Recently, plasmonic cavities in 1D plasmonic structures are being studied both experimentally and theoretically extensively. This section investigates plasmonic band gap formation on 2D square lattice plasmonic structures. We propose a cavity geometry based on the technique which selectively loads the surface with a dielectric layer.

5.2 Fabrication and Experiment

Fabrication of the 2D grating was achieved with an interference lithography setup as we discussed in Chapter 3. The preparation method of the sample is similar to the techniques we discussed in Section 4.2. We, first spin a photosensitive polymer (S1800) on 170 m thick microscope lamella and bake the photosensitive polymer at 110^0C for 1 minute. A He-Cd laser operating at 325 nm was used to record periodic structures on the photosensitive polymer using Lloyd's mirror configuration. To produce 2D gratings, we used double exposure interference lithography. We rotate the sample with a degree of α after the first exposure as shown in Fig.5.1. The angle between the incoming beams , θ, is the same for two exposures so the periods, $\Lambda = 390$ nm, we have recorded during two exposures is the same resulting a square lattice type plasmonic crystals. By this technique, under appropiate rotation angles α and periods Λ it is possible to record rectangular and hexagonal lattices also. Once the structures were developed, a 50 nm thick silver film was evaporated on the samples to support the surface plasmons. The lamella was then mounted on the base of the prism with the metallic side up. Index matching fluid was used between the prism and the lamallae. The BK7 prism allows incoming photons to couple to plasmons. The coupling condition is satisfied at a specific wavelength and angle of incidence given by Eq.4.1. The reflectivity maps are measured and constructed by measuring the coupling wavelength and angle. We used a spectroscopic ellipsometer (VWASE32) for precise reflectivity measurements.

5.3 Diffraction in 2D Plasmonic Crystals

The direct and reciprocal space of 2D square lattice is shown in Fig. 5.2a and Fig. 5.2b respectively. The primitive translation vectors are $a_1 = (a, 0)$ and $a_2 = (0, a)$, these two vectors span all the direct space. The corresponding reciprocal lattice vectors for k-space are $b_1 = \frac{2\pi}{a_1} = 2\pi(\frac{1}{a}, 0)$ and $b_2 = \frac{2\pi}{a_2} = 2\pi(0, \frac{1}{a})$. From the primitive vector of reciprocal lattice, b_1 and b_2, the Brillouin zone can be constructed as a square in Fig 5.2b. We can define the symetry points Γ, M and K. The irreducible Brillouin zone can be constructed as the triangle defined by $\Gamma = (0, 0)$, $M = (\frac{1}{2}, \frac{1}{2})$ and $K = (\frac{1}{2}, 0)$ points in the b_1 and b_2 basis. To characterize the optical properties of the 2D plasmonic crystal, we will concentrate on the in-plane scattering of SPP due to square lattice on the surface. For the general case the scattering condition for SPPs can be written as:

$$k^s_{SPP} = k^i_{SPP} + k_G \tag{5.1}$$

where k^s_{SPP}, k^i_{SPP}, k_G are the wavevector of scattered SPP, the wavevector of incident SPP and the Bragg wavevector of the plasmonic crystal, respectively. k_G is given by $k_G = mb_1 + nb_2$ where m and n equal to -1,1 or 0. We study the

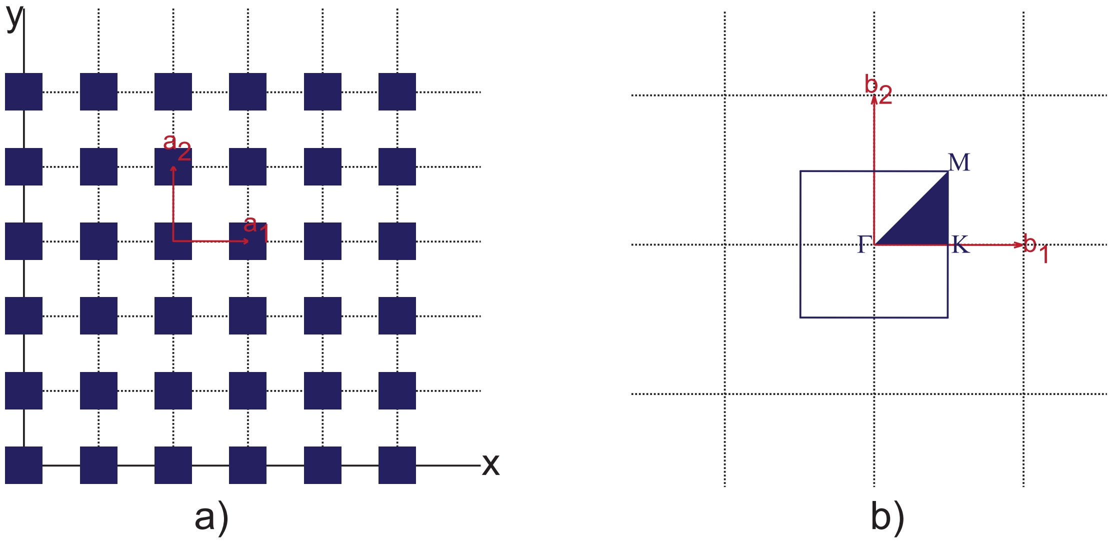

Figure 5.2: a) Schematic direct space of a square lattice b)The first Brillouin zone of a square lattice. Two symetry axes ΓM and ΓK are shown. The irreducible Brillouin zone is shown as blue ΓMK triangle.

scattering conditions in the irreducible Brillouin zone which can be generalized for the whole crystals. The corresponding Bragg wavevector for the irreducible Brillouin zone shown in Fig. 5.2b is $k_G = b_1 + b_2$. SPPs with wavevectors originating from Γ point and terminating on the MK plane satisfy the resonance condition for Bragg scattering. The Bragg condition for SPPs can be written as:

$$\mid k_{SPP} \mid cos(\phi) = \frac{1}{2} \mid b_1 + b_2 \mid \tag{5.2}$$

where ϕ is the angle between the k_{SPP} and ΓM line. The SPPs satisfying the condition above are all Bragg reflected and plasmonic band gaps are opened at those directions. The SPP propagating along the ΓK direction, the center of the gap is found from Eq. 5.2 as:

$$\lambda_{SPP} = 2a \tag{5.3}$$

and for the ΓM direction, corresponding resonance is given by:

$$\lambda_{SPP} = \sqrt{2}a \tag{5.4}$$

We carried on reflection measurements with the above configuration. The orientation of the sample with respect to prism prism is crucial shown in Fig.5.3. By rotating the sample, we can extract the information along any direction. Here

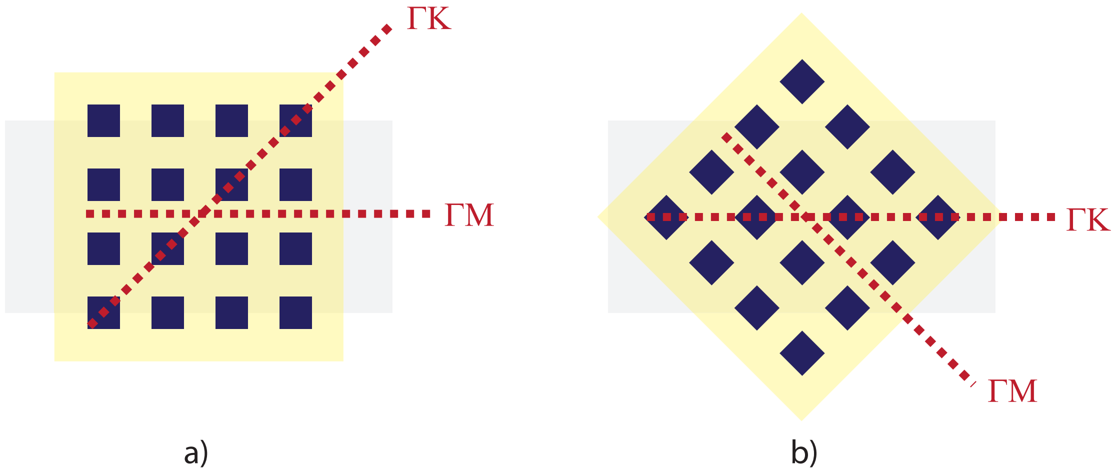

Figure 5.3: Two different orientation of sample with respect to prism surface. a)Excitation of SPP along ΓK axis. b)a)Excitation of SPP along ΓM

we look at two symetry axis ΓK and ΓM. Fig.5.3a depicts the orientation where the reflectivity map of ΓK axis is measured. Note that ΓK axis is parallel to the x-axis. The center of the plasmonic band gap is located at 780 nm. The blue shift for λ_- and red shift for λ_+ is seen as the angle of incidence increases. Rotating the sample with 45^0, ΓM axis is parallel to the x-axis in this case as shown in Fig.5.3b. The reflectivity map of this axis is measured and shown in Fig.5.5. We observed different resonances at these measurements. The expected plasmonic band gap should be centered aroun 558 nm. We observed dips around 551 nm and there are no dips from 563-572nm. We identify that part as the plasmonic band gap along ΓM direction. However, there are additional minimas in the reflecivity maps. This behavior is still being studied.

5.4 Cavity Geometry

Here, we propose the application of the technique which we used to demonstrate plasmonic cavity formation on uniform gratings with 2D crystals. The dielectric layer which will be deposited on the surface will increase the effective index of the SPPs. Then selectively loading the surface will enable localization of SPPs as discussed in Section. 4.3. The geometry of the cavity should be chosen taking

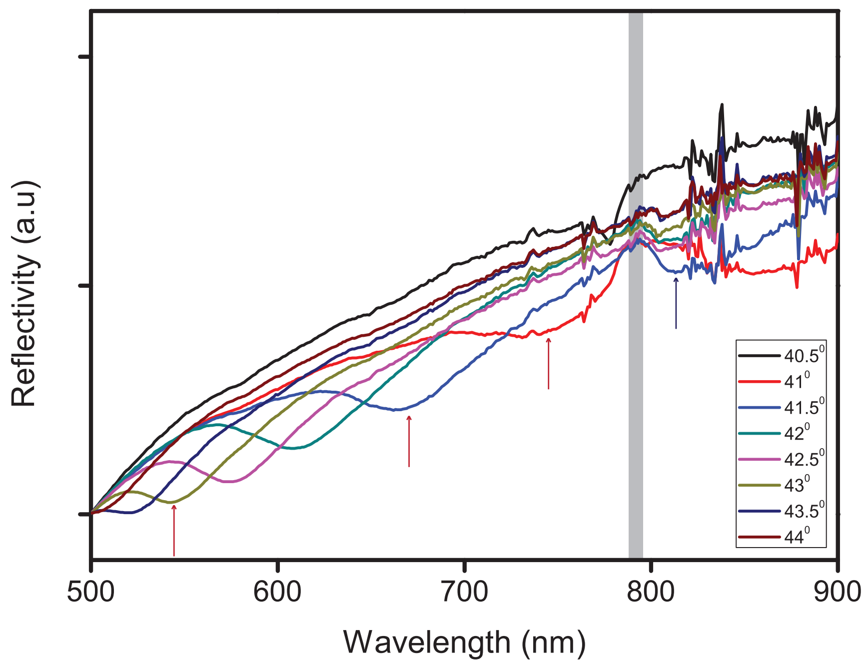

Figure 5.4: The reflectivity maps for different angle of incidences for the ΓK axis

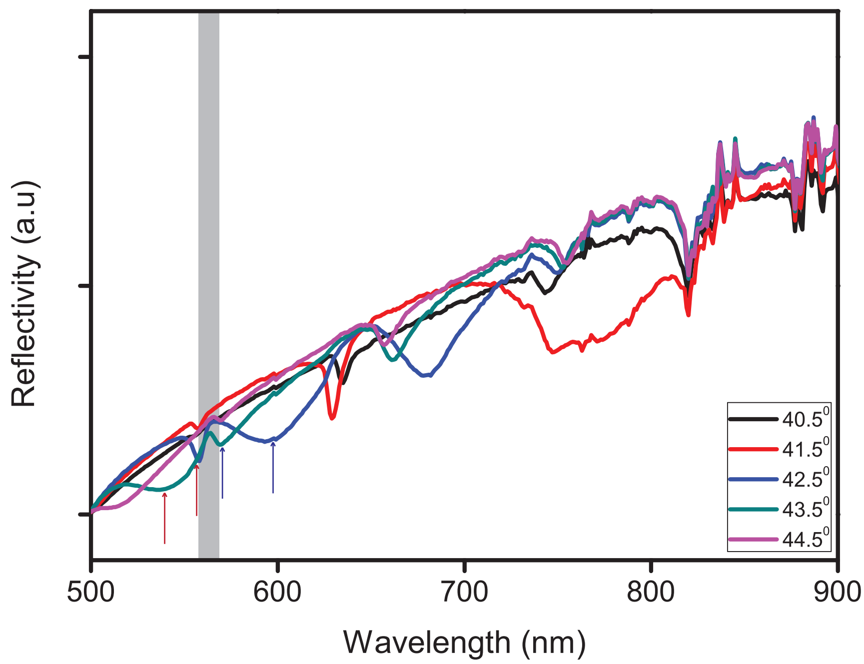

Figure 5.5: The reflectivity maps taken at different angle of incidences for ΓM axis

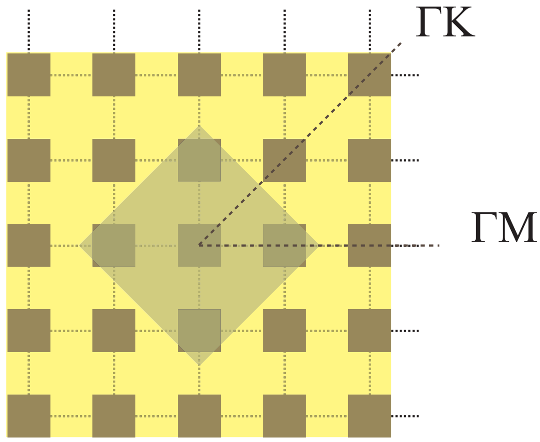

Figure 5.6: The schmatic representation of plasmonic cavity in square lattice

into account Bragg condition along two symetry axis 5.3 and 5.4 and resonance condition Eq. 4.2. We assume that Δn will be constant for a range between the center of the gaps at two symetry axis ΓM and MK. Then the only parameter in Eq. 4.2 changing for symetry axis is the wavelength, λ. Their ratio $\frac{\lambda_{SPP}^{\Gamma K}}{\lambda_{SPP}^{\Gamma M}}$ equals to $\sqrt{2}$. The proposed geometry is the square and the orientation of this square is shown in Fig. 5.6 should be as follows. The diagonal of the cavity should be paralel to the ΓK line.

5.5 Conclusions

In this thesis, we couple to a metallic grating using a prism and tune the band gap by loading the metallic surface with a high index dielectric. Considering that the band gap tunability is an important issue for future device work, demonstration of its control through proper choice of a dielectric is crucial. We also observe that selective use of dielectric loading leads to cavity formation. We have thus designed and fabricated a SPP cavity on a uniform metallic grating through selective loading of the metallic surface with silicon. Spectral reflectivity measurements in the Kretchman configuration permit us to construct the band structures of the samples with and without cavity. A cavity state is observed in approximately the middle of the band gap on samples with the cavity which exists only for a small range of wavelengths and angle of incidences. A detailed analysis of the quality factor of grating based plasmonic cavities is made. Contributions to the Q factor in the cavity are summarized as absorption loss and radiation loss. Metallic absorption loss can only be improved using different metals having low loss coefficients. Radiative loss is dominated by the out-of-plane scattering. We have shown that the loss due to the out-of-plane radiation in the plasmonic band gap cavities on biharmonic gratings can be overcome by decreasing the strength of the grating components inside the cavity. Localization of SPPs in cavities is ultimately related to group velocity control of SPPs where exciting new physics is expected as well as to applications in enhancement of electromagnetic interactions leading to sensors with higher sensitivities. The simple design and fabrication process of the grating based cavities permit mass production of such samples.

Bibliography

[1] WL Barnes, A Dereux, and TW Ebbesen. Surface plasmon subwavelength optics. *NATURE*, 424(6950):824–830, AUG 14 2003.

[2] Harry A. Atwater. The promise of plasmonics. *SCIENTIFIC AMERICAN*, 296(4):56–63, APR 2007.

[3] K Kneipp, Y Wang, H Kneipp, LT Perelman, I Itzkan, R Dasari, and MS Feld. Single molecule detection using surface-enhanced Raman scattering (SERS). *PHYSICAL REVIEW LETTERS*, 78(9):1667–1670, MAR 3 1997.

[4] SM Nie and SR Emery. Probing single molecules and single nanoparticles by surface-enhanced Raman scattering. *SCIENCE*, 275(5303):1102–1106, FEB 21 1997.

[5] K Kneipp, H Kneipp, I Itzkan, RR Dasari, and MS Feld. Surface-enhanced Raman scattering and biophysics. *JOURNAL OF PHYSICS-CONDENSED MATTER*, 14(18):R597–R624, MAY 13 2002.

[6] Jiri Homola. Surface plasmon resonance sensors for detection of chemical and biological species. *CHEMICAL REVIEWS*, 108(2):462–493, FEB 2008.

[7] Stefan A.Maier. *Plamosmonics: Fundamentals and Applications*. Springer, Bath, United Kingdom, 2007.

[8] Frederick Wooten. *Optical Properties of Solids*. Academic Press, United States of America, 1972.

[9] A. R. Zakharian, J. V. Moloney, and M. Mansuripur. Surface plasmon polaritons on metallic surfaces. *OPTICS EXPRESS*, 15(1):183–197, JAN 8 2007.

[10] WL Barnes. Surface plasmon-polariton length scales: a route to subwavelength optics. *JOURNAL OF OPTICS A-PURE AND APPLIED OPTICS*, 8(4, Sp. Iss. SI):S87–S93, APR 2006.

[11] I Avrutsky. Surface plasmons at nanoscale relief gratings between a metal and a dielectric medium with optical gain. *PHYSICAL REVIEW B*, 70(15), OCT 2004.

[12] Charles Kittel. *Introduction to Solid State Physics*. John Wiley Sons, Inc, United States of America, 2005.

[13] Joshua N. Winn John D. Joannopolous, Robert D. Meade. *Photonic Crytsals Molding the Flow of Light*. Princestone University Press, 1995.

[14] WL Barnes, TW Preist, SC Kitson, and JR Sambles. Physical origin of photonic energy gaps in the propagation of surface plasmons on gratings. *PHYSICAL REVIEW B*, 54(9):6227–6244, SEP 1 1996.

[15] J.-C. Weeber, A. Bouhelier, G. Colas des Francs, L. Markey, and A. Dereux. Submicrometer in-plane integrated surface plasmon cavities. *NANO LETTERS*, 7(5):1352–1359, MAY 2007.

[16] Yiyang Gong and Jelena Vuckovic. Design of plasmon cavities for solid-state cavity quantum electrodynamics applications. *APPLIED PHYSICS LETTERS*, 90(3), JAN 15 2007.

[17] Askin Kocabas, S. Seckin Senlik, and Atilla Aydinli. Slowing Down Surface Plasmons on a Moire Surface. *PHYSICAL REVIEW LETTERS*, 102(6), FEB 13 2009.

[18] Askin Kocabas, S. Seckin Senlik, and Atilla Aydinli. Plasmonic band gap cavities on biharmonic gratings. *PHYSICAL REVIEW B*, 77(19), MAY 2008.

[19] Askin Kocabas, Gulay Ertas, S. Seckin Senlik, and Atilla Aydinli. Plasmonic band gap structures for surface-enhanced Raman scattering. *OPTICS EXPRESS*, 16(17):12469–12477, AUG 18 2008.

[20] Marianne Derouard, Jerome Hazart, Gilles Lerondel, Renaud Bachelot, Pierre-Michel Adam, and Pascal Royer. Polarization-sensitive printing of surface plasmon interferences. *OPTICS EXPRESS*, 15(7):4238–4246, APR 2 2007.

[21] Edward D. Palik. *Handbook of Optical Constants of Solids*. Academic Press, 1985.

[22] SC Kitson, WL Barnes, and JR Sambles. Full photonic band gap for surface modes in the visible. *PHYSICAL REVIEW LETTERS*, 77(13):2670–2673, SEP 23 1996.

[23] M Kretschmann and AA Maradudin. Band structures of two-dimensional surface-plasmon polaritonic crystals. *PHYSICAL REVIEW B*, 66(24), DEC 15 2002.

[24] M Notomi. Theory of light propagation in strongly modulated photonic crystals: Refractionlike behavior in the vicinity of the photonic band gap. *PHYSICAL REVIEW B*, 62(16):10696–10705, OCT 15 2000.

[25] A. L. Baudrion, J. C. Weeber, A. Dereux, G. Lecamp, P. Lalanne, and S. I. Bozhevolnyi. Influence of the filling factor on the spectral properties of plasmonic crystals. *PHYSICAL REVIEW B*, 74(12), SEP 2006.

Appendix A

Fundamentals of Finite Difference Time Domain

This chapter reviews the Finite Difference Time Domain technique for solving initial boundary value problems of Maxwell's equations.

Maxwell's equation set for an isotropic medium are:

$$\frac{\partial B}{\partial t} + \nabla \times E = 0 \tag{A.1}$$

$$\frac{\partial D}{\partial t} - \nabla \times H = J \tag{A.2}$$

$$B = \mu H \tag{A.3}$$

$$D = \epsilon E \tag{A.4}$$

$$\tag{A.5}$$

where J,μ and ϵ are defined for every point of the space at any time. The Eq.A.1 and Eq.A.2 results with six sclar equations when we take the curl(∇x) of E and H.

$$-\frac{\partial B_x}{\partial t} = \frac{\partial E_z}{\partial y} - \frac{\partial E_y}{\partial z} \tag{A.6}$$

$$-\frac{\partial B_y}{\partial t} = \frac{\partial E_x}{\partial z} - \frac{\partial E_z}{\partial x} \tag{A.7}$$

$$\frac{\partial B_z}{\partial t} = \frac{\partial E_x}{\partial y} - \frac{\partial E_y}{\partial x} \tag{A.8}$$

$$\frac{\partial D_x}{\partial t} = \frac{\partial H_z}{\partial y} - \frac{\partial H_y}{\partial z} - J_x \tag{A.9}$$
$$\frac{\partial D_y}{\partial t} = \frac{\partial H_x}{\partial z} - \frac{\partial H_z}{\partial x} - J_y \tag{A.10}$$
$$\frac{\partial D_z}{\partial t} = \frac{\partial H_y}{\partial x} - \frac{\partial H_z}{\partial y} - J_z \tag{A.11}$$
$$\tag{A.12}$$

Any field component of space and time can be discretisized as follows:

$$F(i\Delta x, j\Delta y, k\Delta z, n\Delta t) = F^n(i,j,k) \tag{A.13}$$

Then Eq.A.7 can be written as:

$$\begin{aligned}\frac{B_x^{n+1/2}(i,j+\frac{1}{2},k+\frac{1}{2}) - B_x^{n-1/2}(i,j+\frac{1}{2},k+\frac{1}{2})}{\Delta t} \\ = \frac{E_y^n(i,j+\frac{1}{2},k+1) - E_y^n(i,j+\frac{1}{2},k)}{\Delta z} \\ - \frac{E_z^n(i,j+1,k+\frac{1}{2}) - E_z^n(i,j,k+\frac{1}{2})}{\Delta y}\end{aligned} \tag{A.14}$$

similarly Eq.A.10 can be written as

$$\begin{aligned}\frac{D_z^n(i+\frac{1}{2},j,k) - D_x^{n-1}(i+\frac{1}{2},j,k)}{\Delta t} \\ = \frac{H_z^{n-1/2}(i+\frac{1}{2},j+\frac{1}{2},k) - H_z^{n-1/2}(i+\frac{1}{2},j-\frac{1}{2},k)}{\Delta y} \\ - \frac{H_y^{n-1/2}(i+\frac{1}{2},j,k+\frac{1}{2}) - H_y^{n-1/2}(i+\frac{1}{2},j,k-\frac{1}{2})}{\Delta z}\end{aligned} \tag{A.15}$$
$$+J_x^{n-1/2} * (i+\frac{1}{2},j,k) \tag{A.16}$$

Similar expression for Eq.A.8A.9A.11A.12. The grid sizes are chosen such that electromagnetic field does not change significantly in one step. The criteria for the stability is:

$$\sqrt{(\Delta x)^2 + (\Delta y)^2 + (\Delta z)^2} > c\Delta t = \sqrt{\frac{1}{\epsilon\mu}} * \Delta t \tag{A.17}$$

To get accurate results this criteria has to be met. Now we will concentrate on the application of the method in two dimensional systems since we usually have a homogeneous medium along one axis. Here we assume the field components do not depend on the z cordinate.ϵ and μ is constant along the z axis and $J = 0$. The electromagnetic fields can be decomposed into transverse electric(TE) and transverse magnetic(TM) fields. We will show the equations that are solved in the case of TE mode. For TE mode:

$$\begin{aligned} H_x = H_y &= 0 \\ E_z &= 0 \\ -\mu\frac{\partial H_z}{\partial t} &= \frac{\partial E_y}{\partial x} - \frac{\partial E_x}{\partial y}, \\ \epsilon\frac{\partial H_z}{\partial y} &= \frac{\partial E_x}{\partial t} \\ \frac{\partial H_z}{\partial x} &= \epsilon\frac{\partial E_y}{\partial t} \end{aligned} \tag{A.18}$$

We can write the difference equations for TE as:

$$\begin{aligned} H_z^{n+1/2}(i+\frac{1}{2}, j+\frac{1}{2}) - H_z^{n-1/2}(i+\frac{1}{2}, j+\frac{1}{2}) &= \\ -\frac{1}{Z}\frac{\Delta\tau}{\Delta x}[E_n^y(i+1, j+\frac{1}{2}) - E_n^y(i, j+\frac{1}{2})] \\ +\frac{1}{Z}\frac{\Delta\tau}{\Delta y}[E_n^x(i+\frac{1}{2}, j+1) - E_n^y(i+\frac{1}{2}, j)] \end{aligned}$$

$$E_x^{n+1}(i+\frac{1}{2}, j) = E_x^n(i+\frac{1}{2}, j) \tag{A.19}$$

$$+Z\frac{\Delta\tau}{\Delta y}[H_{n+1/2}^z(i+\frac{1}{2}, j+\frac{1}{2}) - H_z^{n+1/2}(i+\frac{1}{2}, j-\frac{1}{2})]$$

$$E_y^{n+1}(i, j+\frac{1}{2}) = \tag{A.20}$$

$$-Z\frac{\Delta\tau}{\Delta x}[H_z^{n+1/2}(i+\frac{1}{2}, j+\frac{1}{2}) - H_z^{n+1/2}(i-\frac{1}{2}, j+\frac{1}{2})] \tag{A.21}$$

These equations are solved step by step when the initial boundary conditions are given. In our case the initial boundary conditions are incident waves such as plasmon filed on metal-air interface or a gaussian beam which is incident on to a prism-air interface.